Solar neutrino measurements in Super-Kamiokande-I

J. Hosaka,[1] K. Ishihara,[1] J. Kameda,[1] Y. Koshio,[1] A. Minamino,[1] C. Mitsuda,[1,*] M. Miura,[1] S. Moriyama,[1] M. Nakahata,[1] T. Namba,[1,†] Y. Obayashi,[1] N. Sakurai,[1,‡] A. Sarrat,[1] M. Shiozawa,[1] Y. Suzuki,[1] Y. Takeuchi,[1] S. Yamada,[1,†] I. Higuchi,[2] M. Ishitsuka,[2,§] T. Kajita,[2] K. Kaneyuki,[2] G. Mitsuka,[2] S. Nakayama,[2] H. Nishino,[2] A. Okada,[2] K. Okumura,[2] C. Saji,[2] Y. Takenaga,[2] S. Clark,[3] S. Desai,[3,‖] E. Kearns,[3] S. Likhoded,[3] J. L. Stone,[3] L. R. Sulak,[3] W. Wang,[3] M. Goldhaber,[4] D. Casper,[5] J. P. Cravens,[5] W. R. Kropp,[5] D. W. Liu,[5] S. Mine,[5] M. B. Smy,[5] H. W. Sobel,[5] C. W. Sterner,[5] M. R. Vagins,[5] K. S. Ganezer,[6] J. Hill,[6] W. E. Keig,[6] J. S. Jang,[7] J. Y. Kim,[7] I. T. Lim,[7] K. Scholberg,[8] C. W. Walter,[8] R. W. Ellsworth,[9] S. Tasaka,[10] G. Guillian,[11] A. Kibayashi,[11] J. G. Learned,[11] S. Matsuno,[11] M. D. Messier,[12] Y. Hayato,[13] A. K. Ichikawa,[13] T. Ishida,[13] T. Ishii,[13] T. Iwashita,[13] T. Kobayashi,[13] T. Nakadaira,[13] K. Nakamura,[13] K. Nitta,[13] Y. Oyama,[13] Y. Totsuka,[13] A. T. Suzuki,[14] M. Hasegawa,[15] I. Kato,[15] H. Maesaka,[15] T. Nakaya,[15] K. Nishikawa,[15] T. Sasaki,[15] H. Sato,[15] S. Yamamoto,[15] M. Yokoyama,[15] T. J. Haines,[16] S. Dazeley,[17] B. K. Kim,[17] K. B. Lee,[17] S. Hatakeyama,[17] R. Svoboda,[17] E. Blaufuss,[18] J. A. Goodman,[18] G. W. Sullivan,[18] D. Turcan,[18] J. Cooley,[19,¶] A. Habig,[20] Y. Fukuda,[21] T. Sato,[21] Y. Itow,[22] C. K. Jung,[23] T. Kato,[23] K. Kobayashi,[23] M. Malek,[23] K. Martens,[23,**] C. Mauger,[23] C. McGrew,[23] E. Sharkey,[23] C. Yanagisawa,[23] N. Tamura,[24] M. Sakuda,[26] Y. Kuno,[25] M. Yoshida,[25] S. B. Kim,[27] J. Yoo,[27,††] H. Okazawa,[28] T. Ishizuka,[29] Y. Choi,[30] H. K. Seo,[30] Y. Gando,[31] T. Hasegawa,[31] K. Inoue,[31] J. Shirai,[31] A. Suzuki,[31] K. Nishijima,[33] H. Ishino,[34] Y. Watanabe,[34] M. Koshiba,[32] D. Kielczewska,[35] J. Zalipska,[35] H. G. Berns,[36] R. Gran,[36] K. K. Shiraishi,[36] A. L. Stachyra,[36] K. Washburnand,[36] and R. J. Wilkes[36]

(Super-Kamiokande Collaboration)

[1]*Kamioka Observatory, Institute for Cosmic Ray Research, University of Tokyo, Kamioka, Gifu 506-1205, Japan*
[2]*Research Center for Cosmic Neutrinos, Institute for Cosmic Ray Research, University of Tokyo, Kashiwa, Chiba 277-8582, Japan*
[3]*Department of Physics, Boston University, Boston, Massachusetts 02215, USA*
[4]*Physics Department, Brookhaven National Laboratory, Upton, New York 11973, USA*
[5]*Department of Physics and Astronomy, University of California, Irvine, Irvine, California 92697-4575, USA*
[6]*Department of Physics, California State University, Dominguez Hills, Carson, California 90747, USA*
[7]*Department of Physics, Chonnam National University, Kwangju 500-757, Korea*
[8]*Department of Physics, Duke University, Durham, North Carolina 27708, USA*
[9]*Department of Physics, George Mason University, Fairfax, Virginia 22030, USA*
[10]*Department of Physics, Gifu University, Gifu, Gifu 501-1193, Japan*
[11]*Department of Physics and Astronomy, University of Hawaii, Honolulu, Hawaii 96822, USA*
[12]*Department of Physics, Indiana University, Bloomington, Indiana 47405-7105, USA*
[13]*High Energy Accelerator Research Organization (KEK), Tsukuba, Ibaraki 305-0801, Japan*
[14]*Department of Physics, Kobe University, Kobe, Hyogo 657-8501, Japan*
[15]*Department of Physics, Kyoto University, Kyoto, Kyoto 606-8502, Japan*
[16]*Physics Division, P-23, Los Alamos National Laboratory, Los Alamos, New Mexico 87544, USA*
[17]*Department of Physics and Astronomy, Louisiana State University, Baton Rouge, Louisiana 70803, USA*
[18]*Department of Physics, University of Maryland, College Park, Maryland 20742, USA*
[19]*Department of Physics, Massachusetts Institute of Technology, Cambridge, Massachusetts 02139, USA*
[20]*Department of Physics, University of Minnesota, Duluth, Minnesota 55812-2496, USA*
[21]*Department of Physics, Miyagi University of Education, Sendai, Miyagi 980-0845, Japan*
[22]*Department of Physics, Nagoya University, Nagoya, Aichi 464-8602, Japan*
[23]*Department of Physics and Astronomy, State University of New York, Stony Brook, New York 11794-3800, USA*
[24]*Department of Physics, Niigata University, Niigata, Niigata 950-2181, Japan*
[25]*Department of Physics, Osaka University, Toyonaka, Osaka 560-0043, Japan*
[26]*Department of Physics, Okayama University, Okayama, Okayama 700-8530, Japan*
[27]*Department of Physics, Seoul National University, Seoul 151-742, Korea*
[28]*International and Cultural Studies, Shizuoka Seika College, Yaizu, Shizuoka 425-8611, Japan*
[29]*Department of Systems Engineering, Shizuoka University, Hamamatsu, Shizuoka 432-8561, Japan*
[30]*Department of Physics, Sungkyunkwan University, Suwon 440-746, Korea*
[31]*Research Center for Neutrino Science, Tohoku University, Sendai, Miyagi 980-8578, Japan*
[32]*The University of Tokyo, Bunkyo, Tokyo 113-0033, Japan*
[33]*Department of Physics, Tokai University, Hiratsuka, Kanagawa 259-1292, Japan*
[34]*Department of Physics, Tokyo Institute for Technology, Meguro, Tokyo 152-8551, Japan*
[35]*Institute of Experimental Physics, Warsaw University, 00-681 Warsaw, Poland*
[36]*Department of Physics, University of Washington, Seattle, Washington 98195-1560, USA*

(Received 30 August 2005; published 1 June 2006)

The details of Super-Kamiokande-I's solar neutrino analysis are given. Solar neutrino measurement in Super-Kamiokande is a high statistics collection of ^{8}B solar neutrinos via neutrino-electron scattering. The analysis method and results of the 1496 day data sample are presented. The final oscillation results for the data are presented also.

DOI: 10.1103/PhysRevD.73.112001 PACS numbers: 14.60.Pq

I. INTRODUCTION

Super-Kamiokande (Super-K, SK) is an imaging water Cherenkov detector, which detects ^{8}B solar neutrinos by electron scattering. Because of its unprecedented fiducial size of 22.5 kt, Super-K has the advantage of making the current highest statistics measurements of solar neutrinos. It enables us to determine, with high precision, measurements of the solar neutrino flux, energy spectrum, and possible time variations of the flux.

Super-K started taking data in April 1996, and the solar neutrino results of the first phase of SK, which ended in July 2001 and is henceforth referred to as "SK-I," are described in this paper. In Secs. II and III, details of the SK detector and its simulation are given. After the event reconstruction method, detector calibration and sources of background are described in Secs. IV, V, and VI, respectively; the data analysis method and results are described in Secs. VII and VIII. Finally, in Sec. IX the solar neutrino oscillation analysis is discussed.

II. SUPER-KAMIOKANDE DETECTOR

A. Detector outline

As has been discussed in much greater detail elsewhere [1], the Super-Kamiokande detector consists of about 50 000 tons of ultrapure water in a stainless steel cylindrical water tank with 11 146 20-inch photomultiplier tubes (PMT's) in the inner detector (ID) and 1885 8-inch PMT's in the outer detector (OD). The diameter and height of the SK tank are 39.3 m and 41.4 m, respectively. The coordinates of the SK tank are defined in Fig. 1. In the inner detector, the active photodetector coverage is 40.4% while the remainder is covered with black, polyethylene terephthalate sheets, generally referred to simply as "black sheet." Signals from PMT's are sent through an electronics chain which can measure both the arrival time of Cherenkov photons as well as the amount of charge they liberate from the phototubes' photocathodes.

The Super-K detector is located 1000 m underground (2700 m of water equivalent) in Kamioka Observatory, deep within the Kamioka mine in Gifu Prefecture, Japan. The Observatory is owned and operated by the Institute for Cosmic Ray Research, a division of the University of Tokyo. The detector's latitude and longitude are 36° 25' N and 137° 18' E, respectively. Compared to ground level, the intensity of muons is reduced by about 10^{-5} at the depth of the SK detector, and yielding a downward-going muon rate through the detector of about 2 Hz.

As radon concentrations in the Kamioka mine air can exceed 3000 Bq/m^3 during the summer season; there are air-tight doors between the Super-K detector area and the

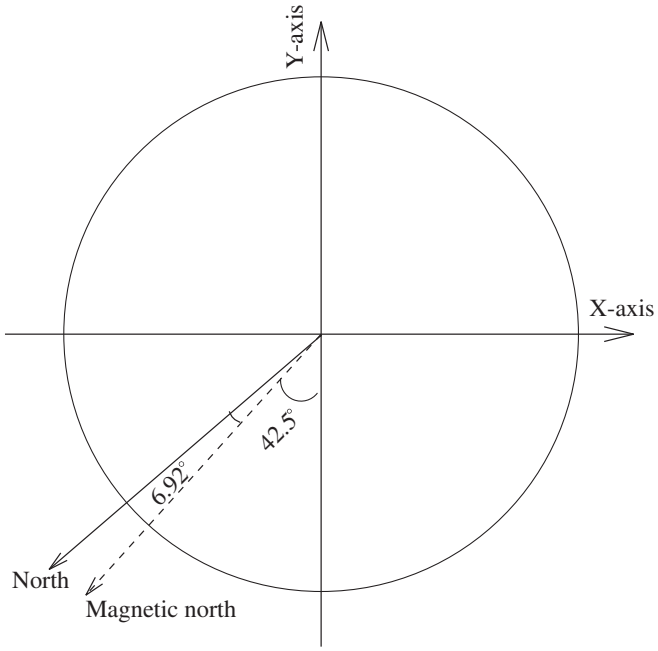

FIG. 1. Coordinates of the Super-Kamiokande detector. The Z axis is defined as the upward direction, pointing away from the center of the earth.

*Present address: High Energy Accelerator Research Organization (KEK), Tsukuba, Ibaraki 305-0801, Japan

†Present address: International Center for Elementary Particle Physics, University of Tokyo, Bunkyo, Tokyo 113-0033, Japan

‡Present address: Faculty of Science, Chiba University, Chiba, Chiba 263-8522, Japan

§Present address: Department of Physics, Indiana University, Bloomington, IN 47405, USA

‖Present address: Center for Gravitational Wave Physics, Pennsylvania State University, University Park, PA 16802, USA

¶Present address: Department of Physics, Stanford University, Stanford, CA 94305, USA

**Present address: Department of Physics, University of Utah, Salt Lake City, UT 84112, USA

††Present address: Fermi National Accelerator Laboratory, Batavia, IL 60510, USA

mine tunnel. The excavated, domed area above the cylindrical water tank, called the ''SK dome,'' is coated with radon-resistant plastic sheets to prevent radon in the surrounding rock from entering the air above the detector. Fresh air from outside the mine is continuously pumped into the SK dome area at the rate of $5 \sim 12$ m^3/minute. As a result, the typical radon concentration in the SK dome air is $20 \sim 30$ mBq/m^3.

As we will see in Sec. VI, radon can lead to background events in the solar neutrino data set. In order to keep radon out of the detector itself, the SK tank is tightly sealed. Radon-reduced air, produced by a special air purification system in the mine, is continuously pumped into the space above the water surface inside the SK tank, maintaining positive pressure. The radon concentration of this radon-reduced air is less than 3 mBq/m^3.

Finally, the purified water in the SK tank is continuously circulated through the water purification system in the mine at the rate of about 35 tons/hour. This means that the entire 50 kt water volume of the detector is passed through the filtration system once every two months or so.

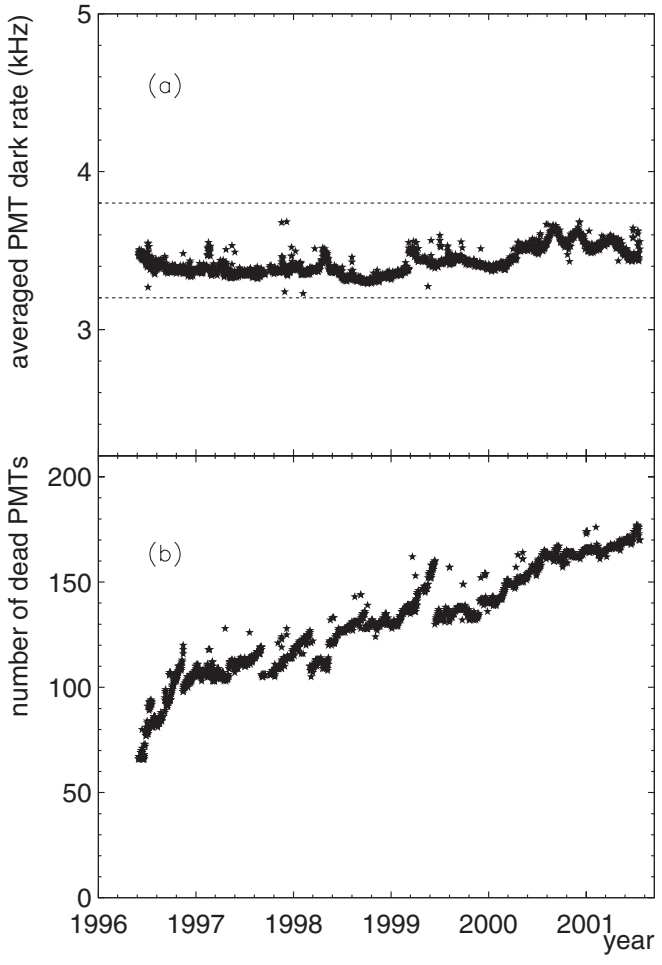

FIG. 2. (a) The average dark noise rate of the PMT's used in SK-I. The dashed lines show the acceptable range for use in the solar neutrino analysis. (b) Number of dead PMT's in SK-I. Note that sometimes repairs were possible, usually involving the replacement of broken high voltage supplies, leading to sudden drops in the number of dead PMT's.

B. Photomultiplier tubes

The PMT's used in the inner part of SK are the 20-inch diameter PMT's developed by Hamamatsu Photonics K. K. in cooperation with members of the original Kamiokande experiment [2]. Detailed descriptions of these PMT's, including their quantum efficiencies, single photoelectron distributions, timing resolutions, and so on, may be found elsewhere [3].

Good timing resolution for light arrival at each PMT is essential for event reconstruction. It is around 3 nsec for single photoelectron light levels.

The dark noise rate of the PMT's is measured to be around 3.5 kHz on average and it was stable over the SK-I data-taking period as shown in Fig. 2(a). The number of accidental hits caused by this dark noise is estimated to be about 2 hits in any 50 nsec time window. For the solar neutrino analysis, this is corrected during the energy calculation as described later in this paper.

Over time some of the PMT's malfunctioned by producing anomalously high dark noise rates or emitting spark-generated light (a tube which makes its own light is called a ''flasher''). The high voltage supplied to these malfunctioning PMT's was turned off shortly after the malfunctions arose, rendering the tubes in question ''dead.'' The number of dead PMT's is shown in Fig. 2(b).

The dark noise rate, plus the numbers of excessively noisy and dead PMT's are taken into account in our Monte Carlo (MC) detector simulation and also corrected for during event reconstruction.

C. Trigger efficiency

A data acquisition trigger is generated whenever a certain number of PMT's are fired within a sliding 200 nsec window. Timing and charge information of each fired PMT is digitized once such a hardware trigger is issued. The ID and OD trigger logic are independent of each other.

When SK-I began data taking in 1996, two threshold levels, called the low energy (LE) trigger and the high energy (HE) trigger, were set in the ID. The threshold number of PMT's for LE and HE triggers were about 29 and 33 PMTs, respectively. This LE hardware trigger threshold corresponded to a 50% triggering efficiency at 5.7 MeV. In order to avoid hardware trigger efficiency issues, the LE *analysis* threshold was ultimately set to 6.5 MeV, where the LE hardware trigger efficiency is essentially 100%.

From May of 1997, a third ID hardware trigger threshold called the super low energy (SLE) trigger was added. Originally set at 24 PMT's, which provided 50% triggering efficiency at 4.6 MeV, the addition of the SLE trigger served to increase the raw trigger rate from 10 Hz to

TABLE I. History of the trigger. The units for rate and livetime are Hz and %, respectively.

Start date	CPUs	Online trigger rate	Filtered trigger rate	Hardware thres. (hits)	Hardware thres. (MeV)	Analysis thres. (MeV)	SLE live time
4/96	0	10	10	29	5.7	6.5	0
5/97	1	120	15	24	4.6	5.0	96.5
2/99	2	120	15	23	4.6	5.0	99.3
9/99	6	580	43	20	4.0	5.0	99.95
9/00	12	1700	140	17	3.5	4.5	99.99

120 Hz. These SLE events were then passed to an online fast vertex fitter, whose operation is described in Sec. IV A.

Since most of these very low energy events are caused by γ's from the rock surrounding the detector and radioactive decay in the PMT glass itself, the fast vertex fitter was used to reject SLE events with event vertices outside the nominal 22.5 kton fiducial volume. This software filtering procedure and its associated online computer hardware was called the Intelligent Trigger, and it filtered the 110 Hz of SLE triggered events down to just 5 Hz of SLE events whose vertices fell within Super-K's fiducial volume. Thus a total event rate of 14.6 Hz was transmitted out of the Kamioka mine for eventual offline reduction and analysis.

In 1999, and again in 2000, the Intelligent Trigger system was upgraded with additional CPU's. By the end of SK-I it provided 100% triggering efficiency at 4.5 MeV and 97% efficiency at 4.0 MeV. Table I shows the history of the trigger as a function of time.

The trigger efficiency was checked with both ^{16}N calibration data from our DT generator, written in Sec. V B 2 in detail, and events from a Ni(n, γ)Ni gamma source. It also

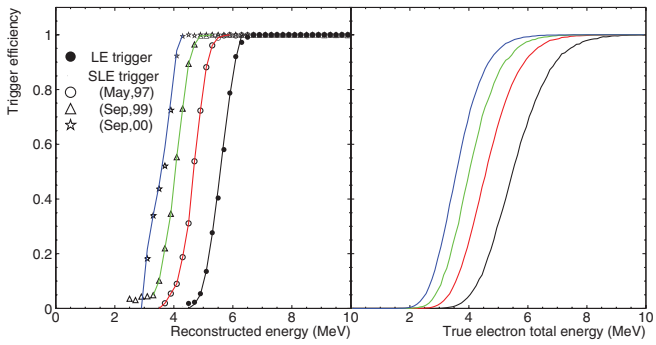

FIG. 3 (color). Trigger efficiency as a function of energy. The left plot shows the efficiency as a function of reconstructed energy (see Sec. IV C for the details of reconstructed energy). The May 1997 LE triggers (black circles with black line) and SLE triggers (white circles with red line) were calculated using a Ni(n, γ)Ni gamma source, while the SLE triggers on September 1999 (triangles with green line) and September 2000 (stars with blue line) were calculated using ^{16}N events from a DT generator. The right plot shows the efficiency as a function of true electron total energy obtained by a Monte Carlo simulation. Identically colored lines represent the same calibration data samples in both plots.

was continuously monitored using prescaled samples of real, unfiltered SLE triggered events. The left plot of Fig. 3 shows the typical trigger efficiency curve as a function of reconstructed energy, which is obtained from the number of hit PMT's after various corrections are applied (see Sec. IV C for more details). The systematic error caused by trigger efficiency is calculated from the difference between data and MC in these DT and Ni calibrations. In order to get the value of this systematic error, we took an average over volume and data-taking time for each trigger condition. A trigger efficiency curve as a function of true electron energy is calculated by a Monte Carlo simulation—it is shown in the right plot of Fig. 3. This plot is for events whose vertices fall within the fiducial volume of the detector (i.e., their true vertex positions are more than 2 m from the PMT wall).

III. SIMULATION

In the simulation of solar neutrino events in Super-Kamiokande-I there are several steps: generate solar neutrinos, determine recoil electron kinematics, generate and track Cherenkov light in water, and simulate response of electronics.

In order to generate the ^{8}B solar neutrino spectrum in Monte Carlo, the calculated spectrum based on the ^{8}B decay measurement of Ortiz *et al.* [4] was used. Figure 4(a) shows the input solar neutrino energy distribution for ^{8}B neutrinos. For the uncertainty in the spectrum we have adopted the estimation by Bahcall *et al.* [5].

In the next step, the recoil electron energy from the following reaction

$$\nu + e \rightarrow \nu + e \tag{3.1}$$

is calculated. Figure 4(b) shows the differential cross section. The (ν_e, e) scattering cross section is approximately 6 times larger than $(\nu_{\mu,\tau}, e)$ because the scattering of ν_e on an electron can take place through both charged and neutral-current interactions, while in the case of $\nu_{\mu,\tau}$ only neutral-current interactions take place. The radiative corrections in the scattering are considered also [6]. Figure 4(c) shows the expected spectrum of recoil electrons in SK without neutrino oscillations. The uncertainty in these cross sections is discussed in [6]. For the calculation of systematic error arising from the ^{8}B solar neutrino

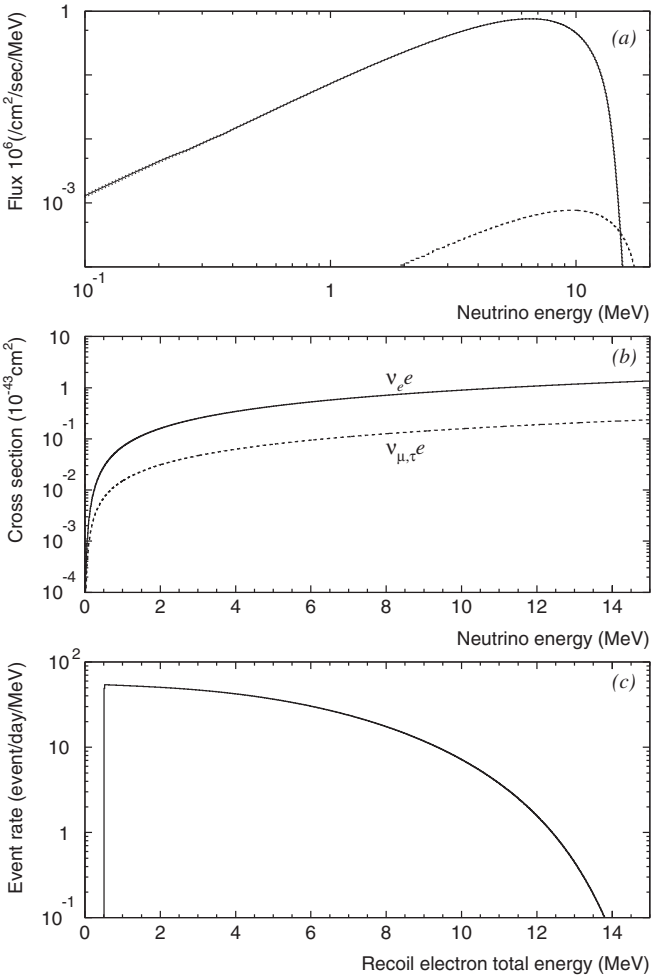

FIG. 4. (a) Input distributions of ^{8}B (solid line) and hep (dashed line) solar neutrino energies. (b) The cross section of the interaction for ν_e (solid line) and $\nu_{\mu,\tau}$ (dashed line) with electrons as a function of neutrino energy. (c) The spectrum of recoil electrons scattered by ^{8}B and hep solar neutrinos.

and neutrino scattering cross section uncertainties, we assume the maximum and minimum value within the uncertainty in each input parameter and use them to calculate the expected fluxes. The errors were then assigned by comparing these shifted values with the corresponding central values.

Assuming the ^{8}B flux of BP2004 [7] (5.79×10^6 /cm^2/ sec) and before taking into account the detector's trigger requirements, the expected number of ν_e scatter events in SK is 325.6 events per day. MC events are generated assuming a rate of 10 recoil electron events per minute for the full operation time of SK-I, yielding a total of 24 273 070 simulated solar neutrino events.

We have used GEANT3.21 for simulation of particle tracking through the detector. Since the tracking of Cherenkov light is especially important in the Super-K detector, parameters related to photon tracking are fine-tuned through the use of several calibration sources.

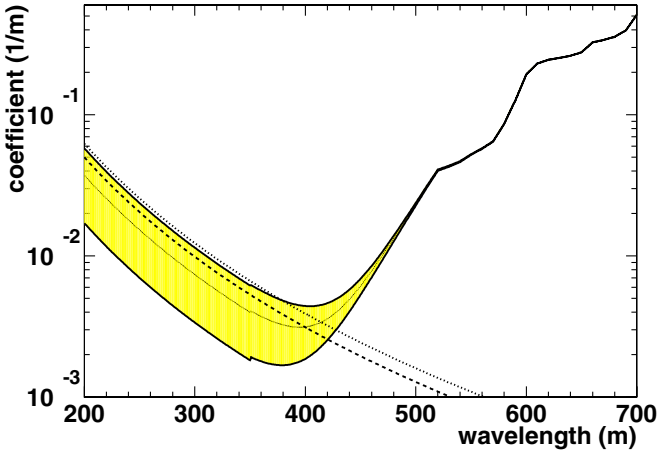

FIG. 5 (color online). Wavelength dependence of the water parameter coefficients: absorption (solid line), Rayleigh scattering (dashed line) and Mie scattering (dotted line). The absorption coefficient is also a function of water transparency. The filled region shows the range of this parameter as water transparency is changed, where the two solid lines define the SK-I minimum (73 m) and maximum (98 m) values.

Figure 5 shows the wavelength dependence of various water coefficients in our MC. Rayleigh scattering is dominant at short wavelengths with a $1/\lambda^4$ dependence. The λ dependence of absorption and Mie scattering are empirically set to $1/\lambda^4$ at shorter wavelengths, while the absorption for longer wavelengths are taken from a separate study [8]. The absorption and scattering coefficients in MC are tuned using LINAC calibration data (see Sec. V B 1) so as to match the MC and data energy scale in each position in the detector.

The water quality in SK changes as a function of time as shown in Fig. 17; this change in water quality was taken into account in the MC simulation. By comparing photon arrival timing distributions using calibration data, it was found that the change in water attenuation length is mainly due to change in the absorption coefficient. So, we fixed Rayleigh scattering and Mie scattering coefficients to be constant over the entire data-taking period and vary only the absorption coefficient in the MC simulation. Figure 6 shows the result. The solid line shows the translation of water transparency into the absorption coefficient. The lower panel shows the deviation of the peak of the reconstructed energy from the peak of the input energy as a function of water transparency—the deviation is less than $\pm 0.2\%$. The coefficients of each process at shorter wavelength are summarized as follows:

$$8.00 \times 10^7/\lambda^4 \text{ [nm]} \quad (1/\text{m}):\text{Rayleigh scat.},$$

$$1.00 \times 10^8/\lambda^4 \text{ [nm]} \quad (1/\text{m}):\text{Mie scat.},$$

$$(2.74 \sim 9.27) \times 10^7/\lambda^4 \text{ [nm]} \quad (1/\text{m}):\text{absorption}.$$

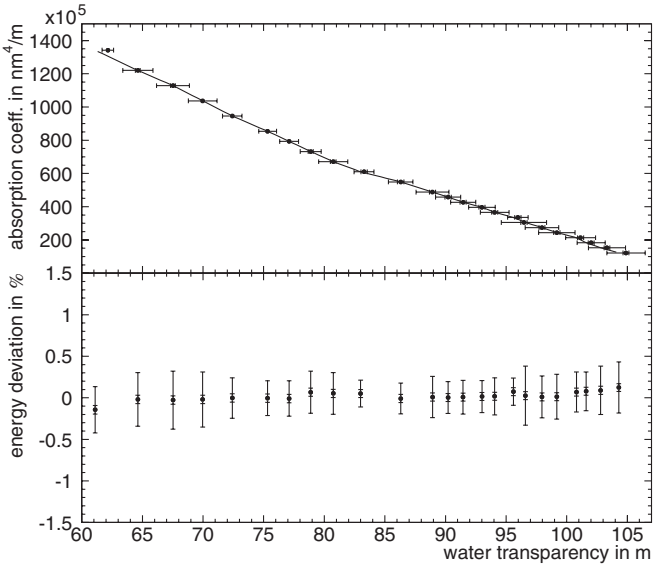

FIG. 6. Translation of the water transparency parameter into a short wavelength absorption coefficient. Absorption is taken to be proportional to λ^{-4} for these wavelengths. Light scattering is assumed to be constant. The lower panel shows the energy deviation as a function of input momentum. The inner error bar of each point is the statistical uncertainty, while the outer error bar represents the spread of the six samples using 5, 6, 8, 10, 12, and 15 MeV/c as the input momenta.

IV. EVENT RECONSTRUCTION METHOD

A. Vertex

Electrons in the energy region of interest for solar neutrinos (below 20 MeV) can travel only a few centimeters in water, so their Cherenkov light is approximately a point source. The reconstruction of this vertex relies solely on the relative timing of the ''hits,'' i.e., PMT's struck by one or more Cherenkov photons. Since the number of observed Cherenkov photons and therefore the likelihood of a multiple hit PMT is comparatively small, about seven recorded photons per MeV of deposited energy, the pulse heights of the hits typically follows a one photoelectron distribution and yields no information about the light intensity nor the distance to the source. For the same reason it is also impossible to separate reflected or scattered Cherenkov photons and PMT dark noise from direct light based upon PMT pulse height. The vertex reconstruction assumes that a photon originating from vertex $\vec{v}$ and ending in hit $\vec{h}_i$ is traveling on a straight path and therefore takes the time $|\vec{v} - \vec{h}_i|/c$ where c is the group velocity of light in water (about 21.6 cm/nsec). Therefore, assuming only direct light, the effective hit times $\tau_i = t_i - |\vec{v} - \vec{h}_i|/c$ at vertex $\vec{v}$ of all PMT's should peak around the time of the event with the width of the PMT timing resolution for single photoelectrons (about 3 nsec). Light scattering and reflection (as well as dark noise, prepulsing and afterpulsing of the PMT's) introduces tails in the distribution which will strongly bias the reconstruction if a χ^2 is used to evaluate the goodness of fit g for a given vertex. Therefore, we use a ''truncated χ^2''

$$g(\vec{v}) = \sum_{i=1}^{N} e^{-(1/2)[(\tau_i - t_0)/\sigma_t]^2}, \tag{4.1}$$

where t_0 is the center of a 10-nsec wide search window in τ which maximizes the number of hits inside. The vertex is reconstructed by the maximization of this goodness varying $\vec{v}$.

We use three different vertex reconstruction algorithms. Our standard vertex fit is used to reconstruct event direction and energy and to compute the likelihood of an event to be due to spallation. Only events inside the fiducial volume (2 m away from the closest PMT) are considered. The Super-K background rate below about 7 MeV rises rapidly with falling energy; most of this background is due to light emanating from or near the PMT's themselves and is reconstructed outside the fiducial volume. However, the rate of misreconstructed events (background events outside the fiducial volume which get reconstructed inside) increases rapidly with falling energy due to long resolution tails. We therefore reconstruct the vertex using a second vertex fitter whose vertex distribution has smaller tails and then accept only events reconstructed inside the fiducial volume by *both* fits. To reduce the rate of SK events stored to tape, we remove SLE events which reconstruct outside of the fiducial volume online. Unfortunately, both offline fitters are too slow to keep up with the trigger rate (see Sec. II A) of SLE events and so we are forced to use a fast reconstruction to prefilter these events. If the vertex of the fast online fit is inside the fiducial volume the event is reconstructed later by the other two fits.

To ensure convergence of the maximum search, the standard fit first evaluates the vertex goodness on a Cartesian grid (see Fig. 7). For a reasonably speedy search in spite of Super-Kamiokande's large size, a coarse grid of 57 points with a grid constant of 397.5 cm is chosen for the xy plane with nine such layers in z separated by 380 cm. Since the grid is coarse, the timing resolution σ_t is artificially set to 10 nsec to smear out the maximum goodness. After the single coarse grid point with the largest goodness is identified, the goodness is calculated at the 27 points of a $3 \times 3 \times 3$ cube centered on this grid point with a timing resolution of $\sigma_t = 5$ nsec and a spatial grid separation of 156 cm. If the largest resulting goodness is not in the center, the cube is shifted so that the largest goodness is in the center of the new cube. Otherwise, the cube is contracted by a factor of 2.7. If the spatial grid separation of the cube reaches 5 cm the maximum search is finished and the reconstructed vertex is the point with the largest found goodness.

To limit the bias of the vertex reconstruction due to the tails in the timing residuals $\tau_i - t_0$, the hits that go in the vertex fit are selected. Since the event vertex is not known,

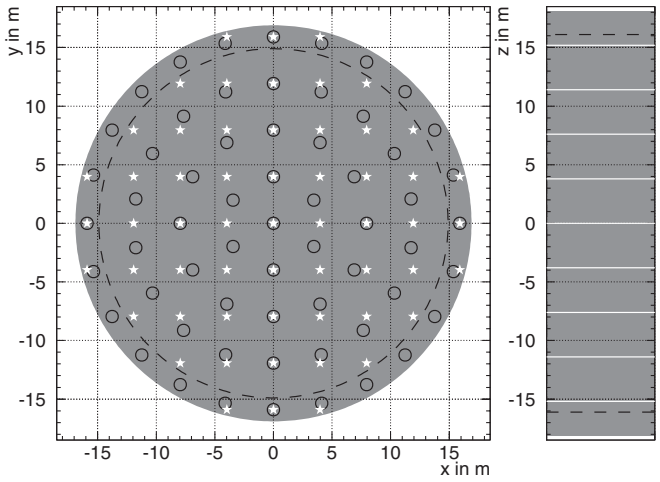

FIG. 7. Search grid for the vertex reconstruction in the xy plane (left figure) and in z (right figure). The shaded area is the SK inner detector volume. The dashed line indicates the fiducial volume. The white stars (left) and white lines (right) are the grid points used by the standard vertex reconstruction. The circles in the xy plane are the points used by the second vertex reconstruction.

the hit selection must be based on the absolute hit times t_i (and the spatial distribution of the hits $\vec{h}_i$). The hit selection of the standard reconstruction first finds the start time of a sliding 200 nsec window (the time required for a photon to cross the diagonal of the detector) which contains the largest number of hits. The rate of late/early hits (background) per nsec is determined by counting the hits outside the window. From this rate, the background inside the window is estimated. The size of the window is then reduced in an attempt to optimize the direct light signal divided by the square root of the late/early hit background. The hits in the resulting, optimal timing window are those selected to compute the vertex goodness.

The second vertex reconstruction (to reduce misreconstructed events originating from the PMT's) modifies the hit selection and the search grid. For two direct light hits i and j, the timing difference Δt_{ij} is limited to $\Delta t_{ij} < |\vec{h}_i - \vec{h}_j|/c$ (see Fig. 8). We select the largest set of hits whose hit pairs obey $\Delta t_{ij} < |\vec{h}_i - \vec{h}_j|/c$ after eliminating ''isolated hits'' (hits which are further away than 1250 cm or further away than 35 nsec from the nearest neighboring hit). With these selected hits we perform a grid search with a circular grid of 60 points on the xy plane (grid constant 397.5 cm) and nine such planes in z separated by 380 cm with a timing resolution of 9.35 nsec. The best-fit point is interpolated from the grid points with the largest goodness. After that, 27 points of a cylindrical section around that point with an initial grid constant of 147.1 cm and 5 nsec resolution are tested. As in the standard reconstruction, the section is moved (if the center point does not have the largest goodness) or reduced in size by a factor of 0.37 (if it does), and the search is finished once the grid constant falls below 5 cm.

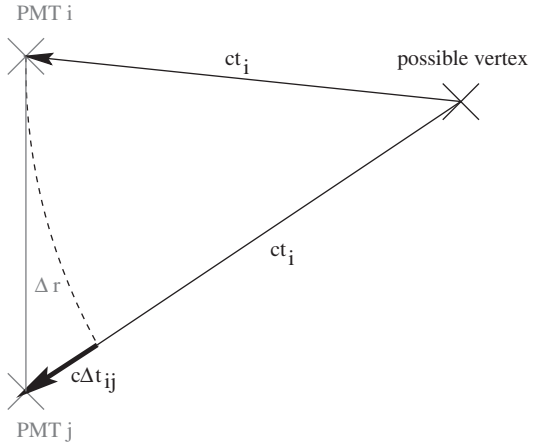

FIG. 8. Timing constraint for pairs of hits. From the triangle relation $ct_i + \Delta x > ct_j = ct_i + \Delta ct_{ij}$ follows $\Delta t_{ij} < \Delta x/c = |\vec{h}_i - \vec{h}_j|/c$.

The fast fit, used to prefilter SLE events online, also eliminates isolated hits (i.e., all other hits separated by either more than 10 m or more than 33.3 nsec) to reduce the effects of dark noise and reflected or scattered light. Then the absolute peak time is estimated by maximizing the number of PMT hits within a 16.7-nsec wide sliding timing window. PMTs that are in the interval ($-$ 33.3 ns, 100 nsec) with respect to the peak time are selected. An initial vertex is calculated by shifting a simple average of the selected PMT positions 2 m toward the detector's center. The time at the event vertex is also determined; this time must be smaller than the absolute peak time yet

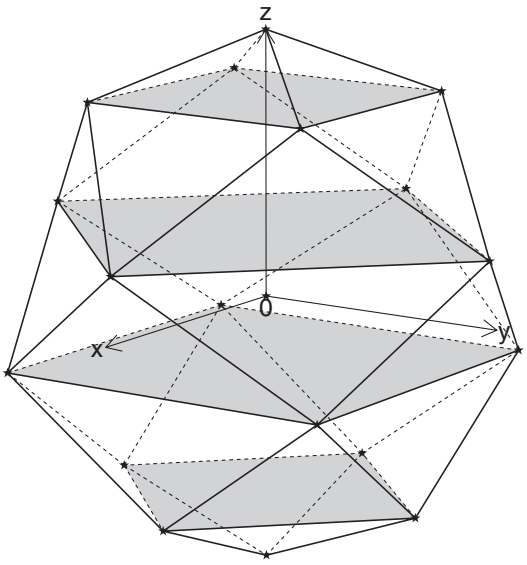

FIG. 9. Search grid for the fast fit. 18 points around the input vertex are tested, the orientation is fixed. The grid size is adjusted between 1 and 8 m (see Table II).

TABLE II. Search parameters for the fast fit.

Step	Size (cm)	$t_0 \pm \sigma_t$ (ns)	$a_0 \pm \sigma_a$	$t_{\rm win}$ (ns)
1	800	2.1 ± 10.2	0.534 ± 0.134	(− 66.7, 100.0)
1		2.7 ± 6.1	0.534 ± 0.134	(− 40.0, 66.7)
2	400	2.3 ± 6.0	0.534 ± 0.134	(− 33.3, 50.0)
3–5		2.3 ± 6.0	0.534 ± 0.134	(− 25.0, 33.3)
1		1.5 ± 4.7	$0.1g$ for $a < 0.2$, $a \geq 0.9$	(− 20.0, 33.3)
2	200	2.2 ± 4.5	g for $0.3 \leq a < 0.85$	(− 20.0, 33.3)
3–5		1.1 ± 4.1	$0.5g$ otherwise	(− 20.0, 26.7)
1–8	100	0.6 ± 3.2	none	(− 13.3, 16.7)

not differ from it by more than 117 nsec. The initial vertex time is chosen to be 58.3 nsec before the absolute peak time. It is then corrected to the average of all time-of-flight subtracted PMT times that are in the interval (− 133.3 ns, 200 nsec) around the initial time. The magnitude of the anisotropy

$$\vec{a} = \frac{\sum_{\text{selected hits}} q_i(\vec{h}_i - \vec{v})/|\vec{h}_i - \vec{v}|}{\sum_{\text{selected hits}} q_i} \tag{4.2}$$

also is calculated at this stage. Next, 18 points around the initial vertex are tested with an initial search radius of 8 m (see Fig. 9), while the goodness g is modified to take into account the anisotropy. At first, the goodness is multiplied by the factor $e^{-0.5((a-a_0)/\sigma_a)^2}$. Later in the search, this factor is replaced by a table. The times are shifted by the expected mismatch between the average vertex time and the vertex peak time t_0. Only hits inside a time interval around the shifted vertex time are considered. The search radii, time shifts, time resolutions, anisotropy factors, and time intervals are listed in Table II.

As shown in Figs. 10 and 11, the performance of all three fitters is evaluated using ^{8}B Monte Carlo. The distribution of the distance between the reconstructed and correct vertex is analyzed for each fit (see Fig. 10); the vertex resolution is extracted as the distance which contains 68.2% of all reconstructed vertices. For recoil electrons above 4.5 MeV, the fast fit shows the worst resolution (115 cm). However, it has the lowest rate of very distant misfits (> 30 m). The resolution of the standard fit is 102 cm, while the second fit's resolution is 94 cm. Figure 11 shows the vertex resolution as a function of generated total recoil electron energy. Since the vertex reconstruction occasionally fails (due to a number of se-

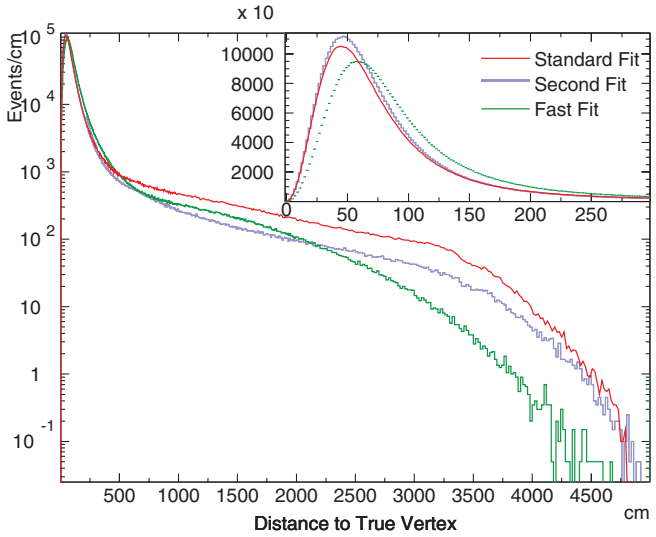

FIG. 10 (color). Distance from reconstructed to correct vertex for ^{8}B Monte Carlo events with total recoil electron energy above 4.5 MeV. The inserted panel magnifies the distributions near zero on a linear scale.

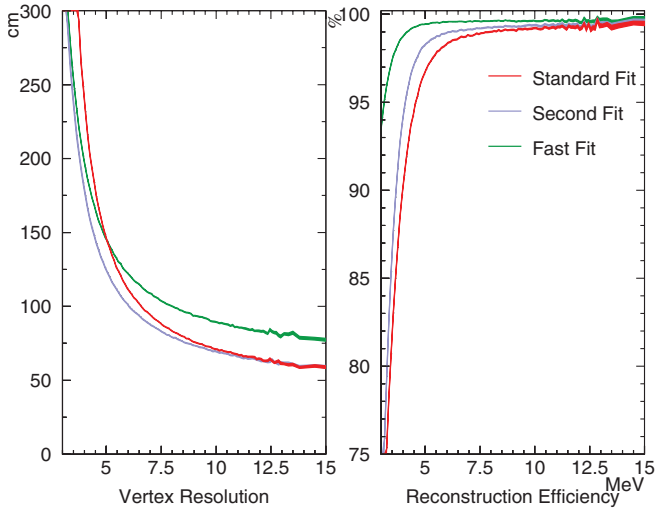

FIG. 11 (color). Vertex resolution (68.2% of reconstructed events reconstruct inside a sphere of radius σ from correct vertex) of ^{8}B Monte Carlo events as a function of total recoil electron energy. The curves on the right-hand side show the fraction of reconstructed events as a function of total recoil electron energy.

lected hits that is too small), the efficiency to reconstruct the event anywhere at all is also plotted.

B. Direction

Since the recoil electron preserves the direction of the solar neutrino, directional reconstruction is important for solar neutrino analysis. This characteristic directionality is used to extract the solar neutrino signal in Super-K. To calculate the direction, a maximum likelihood method using the Cherenkov ring pattern is adopted. The likelihood function is

$$L(\vec{d}) \equiv \sum_{i}^{N_{30}} \log(f(\cos\theta_{\rm dir}))_i \times \frac{\cos\theta_i}{a(\theta_i)}, \qquad (4.3)$$

where N_{30} is the number of hit PMT's with residual times within a 30 nsec window and $f(\cos\theta_{\rm dir})$ is the function that represents the distribution of the opening angle between the particle direction and the vector from the reconstructed vertex to the hit PMT position made by MC. A plot of $f(\cos\theta_{\rm dir})$ for 10 MeV electrons is shown in Fig. 12. The distribution is broad with the peak at 42° because of the effects of electron multiple scattering and Cherenkov light scattering in water. θ_i is the opening angle between the direction of the vector from the reconstructed vertex to the ith hit PMT position and the direction that PMT is facing. $a(\theta_i)$ is the acceptance of PMT's as a function of θ_i which is made by MC. The direction is reconstructed as Eq. (4.3) becomes maximum using a grid search method whose step sizes are 20°, 9°, 4°, 1.6°.

The quality of the directional reconstruction is estimated from the differences between the generated and reconstructed directions using MC. Figure 13 shows the directional resolution dependence on energy within the fiducial volume; it uses directions which are generated uniformly.

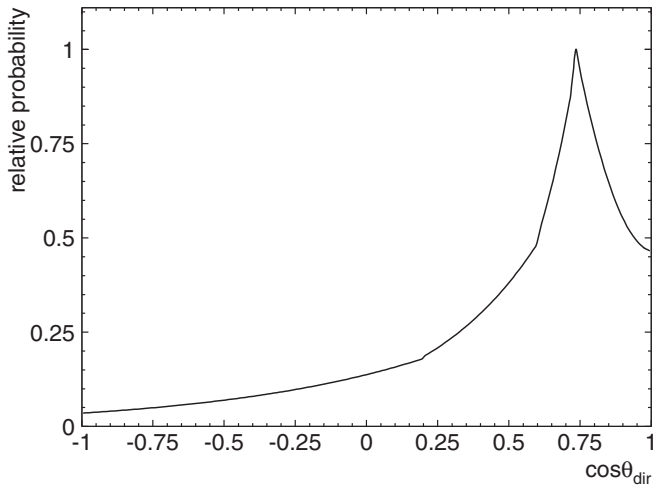

FIG. 12. The distribution of the opening angle between the direction of the generated particle and the vector from the reconstructed vertex to the hit PMT position. This plot is made for 10 MeV electron MC events.

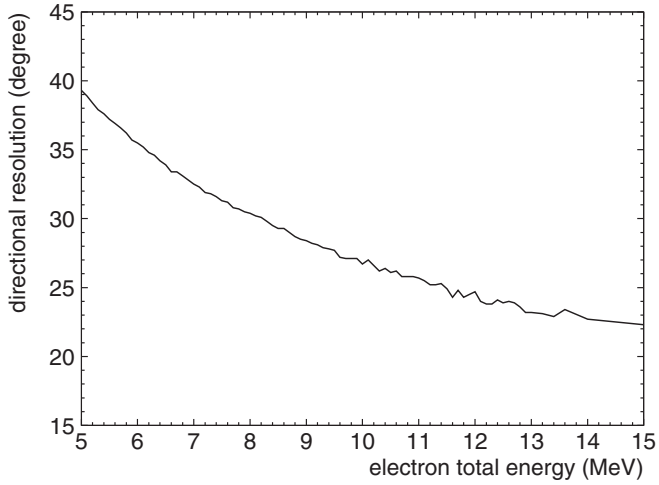

FIG. 13. The directional resolution's dependence on energy, determined using Monte Carlo events.

Here, the resolution is defined as the 68% point for the angle difference distribution. The angular resolution for 10 MeV electrons is about 25°.

C. Energy

The energy of a fully contained charged particle in Super-Kamiokande is approximately proportional to the number of generated Cherenkov photons, and thus is also proportional to the total number of photoelectrons in the resulting hit PMT's. When the particle's energy is low it is also proportional to the number of hit PMT's because in such a case the number of Cherenkov photons collected by any given PMT is almost always zero or one. In order to avoid the effect of noise hits with higher charge, the number of hit PMT's ($N_{\rm hit}$) with some corrections is used for energy determination for the solar neutrino analysis. In order to reject accidental hits due to dark noise in the PMT's, only the hit PMT's with residual times within a 50 nsec window are used for calculating $N_{\rm hit}$. Moreover, we applied several corrections to $N_{\rm hit}$, yielding an effective number of hits ($N_{\rm eff}$) which has the same value at every position in the detector for a given particle energy. These corrections account for the variation of the water transparency, the geometric acceptance of each hit PMT, the number of bad PMT's, the PMT dark noise rate, and so on. The equation for $N_{\rm eff}$ is

$$N_{\rm eff} = \sum_{i=1}^{N_{\rm hit}} \left\{ (X_i + \epsilon_{\rm tail} - \epsilon_{\rm dark}) \times \frac{N_{\rm all}}{N_{\rm normal}} \times \frac{R_{\rm cover}}{S(\theta_i, \phi_i)} \times \exp\left(\frac{r_i}{\lambda(\rm run)}\right) \times G_i(t) \right\}, \qquad (4.4)$$

where X_i is an occupancy used to estimate the effect of multiple photoelectrons, $\epsilon_{\rm tail}$ is the correction for late hits outside the 50 nsec window, and $\epsilon_{\rm dark}$ is for dark noise correction. The definition of X_i is as follows:

$$X_i = \begin{cases} \frac{\log\frac{1}{1-x_i}}{x_i} & x_i < 1 \\ 3 & x_i = 1, \end{cases} \tag{4.5}$$

where x_i is the ratio of the number of hit PMT's to the total number of PMT's in a 3×3 patch around the ith hit PMT. This correction estimates the number of photons which arrived at the ith hit PMT by using the number of hit PMT's surrounding it. Here, the ratio of the unhit PMT's in this patch of nine tubes is $1 - x_i$.

The second factor is the bad PMT correction, where N_{all} is the total number of PMT's, 11 146, and N_{normal} is the number of properly operating PMT's for the relevant subrun.

The third factor is the effective photo coverage. The average of the photo coverage, which is the ratio of the area covered by PMT's to all inner detector area, is $R_{\mathrm{cover}} = 0.4041$. However, the effective photo coverage changes with the incident angle of the photon to the PMT. Therefore, we applied a coverage correction, where $S(\theta_i, \phi_i)$ is the photo coverage from the directional vantage point of θ_i, ϕ_i. Figure 14 shows this function.

The fourth factor is the water transparency correction, where r_i is the distance from the reconstructed vertex to the ith hit PMT position, and λ is water transparency.

The fifth factor, $G(t)_i$, is the gain correction at the single photoelectron level as a function of the time of the manufacture of each PMT.

Finally, the conversion function from N_{eff} to energy is determined by uniformly generated Monte Carlo vertices. This is total energy; all mention of ''energy'' hereafter refers to total energy, i.e. including the scattered electron's rest mass and momentum. The relation to energy is calculated by the following equation:

$$\mathrm{E} = \alpha + \beta N_{\mathrm{eff}}(1 - \gamma N_{\mathrm{eff}}(1 - \delta N_{\mathrm{eff}}(1 - \epsilon N_{\mathrm{eff}}))). \tag{4.6}$$

Here $\alpha = 0.735$, $\beta = 0.134$, $\gamma = 6.049 \times 10^{-4}$, $\delta = 6.441 \times 10^{-3}$, and $\epsilon = 1.541 \times 10^{-3}$. The typical conversion factor from N_{eff} to energy is 6.97. The energy resolution also is estimated by the same MC described above. Figure 15 shows the energy resolution as a function of energy; it is 14.2% for 10 MeV electrons.

D. Muon

Precise reconstruction of cosmic ray muon tracks which penetrate the Super-K detector is needed for the solar neutrino analysis. This is because nuclear spallation events induced by these cosmic ray muons are a dominant background to the solar neutrino signal, and the correlation in time and space between spallation events and their parent muons is extremely useful in rejecting the spallation background. Hence, the track position precision requirement for our muon fitter is about 70 cm since the vertex resolution for low energy events with energies around 10 MeV is also about 70 cm.

The muon fitter has three components; an ''initial fitter,'' a ''TDC fitter,'' and a ''geometric check.''

The initial fitter assumes the position of the first fired PMT is the entrance point of a cosmic ray muon, and the center of gravity of the saturated tubes' positions as the exit point. The PMT at the exit point has the most photoelectrons (p.e.'s) of all PMT's; the expected value is up to 500 p.e. However, our front end electronics saturate at $\sim$230 p.e. in a single tube, and so typically several dozen PMT's near the exit point are saturated. Therefore, the reconstructed exit point is not the position of the most-hit

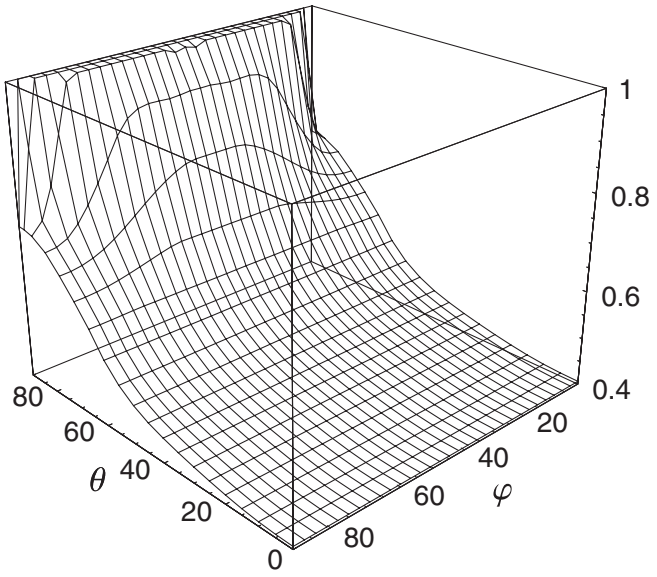

FIG. 14. Function of the effective photo coverage's dependence on the incident angle to a PMT.

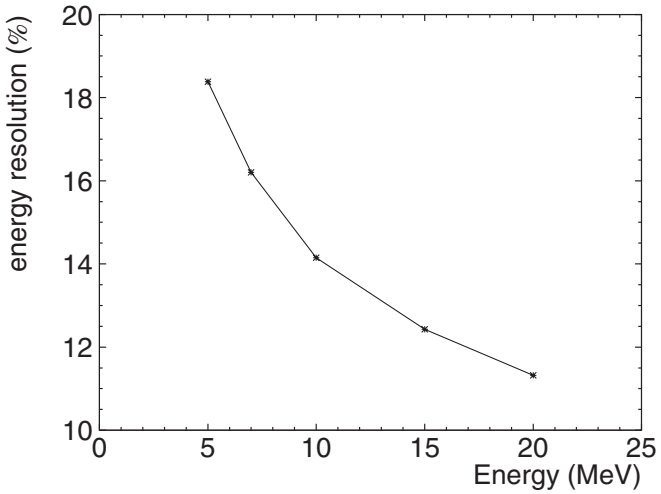

FIG. 15. The energy resolution's dependence on energy as determined using Monte Carlo events.

PMT, but rather the center of gravity of the saturated tubes' positions.

For the entrance position search, we consider the dark noise of the PMT's. For SK-I the dark noise rate of a typical PMT was $\sim$3.5 kHz, though it could rise to $>$10 kHz in the case of a "noisy PMT." In the initial fitter, the following methods are used to reject dark noise hits:

(1) *Charge information of PMT.*—The fitter requires that the PMT at the entrance point have more than 2 p.e., because typical dark hit PMT's have less than 1 p.e. while the amount of charge which they receive from a muon is several p.e.'s.

(2) *Timing information of eight neighbor PMT's.*—Cosmic ray muons emit lots of Cherenkov light ($\sim$ 340 photons/cm), so several PMT's near the entrance point should record photons at the same time. The fitter therefore requires that the PMT at the entrance point have more than five fired neighbor PMT's within 5 nsec.

The results of the initial fitter are then used as initial values by the next stage.

The TDC fitter is a fitter based on a grid search method using timing information. In this fitter, a goodness of fit also is defined to obtain the best track of the muon:

$$g(\vec{v}) = \sum_{i=1}^{N} e^{-(1/2)[(\tau_i - t_0)/(f\times\sigma_t)]^2}, \qquad (4.7)$$

where the definitions are the same as for the "truncated χ^2" in Sec. IV A except for the factor (f), which is found to be 1.5 by Monte Carlo. The TDC fitter surveys a circle of radius 5.5 m from the exit point obtained by initial fitter and then obtains the direction which maximizes the goodness.

The muon fitter determines the muon track by using two independent parameters, timing and charge, and the two results are sometimes different. For example, in the case of muon bundle events, PMT's near the exit point fire at early times, because the velocity of a cosmic ray muon is faster than that of light in water. As a result of these early hits, the exit point can sometimes be mistaken for an entrance point. In order to reject this kind of misfit, the geometric check fitter estimates the consistency of both previous fitters by requiring the following after the TDC fit:

(i) There is no saturated PMT within 3 m from the entrance point.

(ii) There should be some saturated PMT within 3 m from the exit point.

The muon events which do not satisfy these requirements are regarded as failed reconstructions.

We estimated the performance of the muon fitter by using Monte Carlo events. Figure 16 shows the vertex and angular resolutions. For the entrance point, the 1-σ vertex resolution is estimated to be 68 cm. This value corresponds closely to the spacing interval between each PMT, 70.7 cm. The vertex resolution of exit point is 40 cm, Therefore, the distance between the actual muon track and the fitted one is estimated to be less than 70 cm, which means that this muon fitter satisfies our precision requirement. The angular resolution is estimated to be 1.6°.

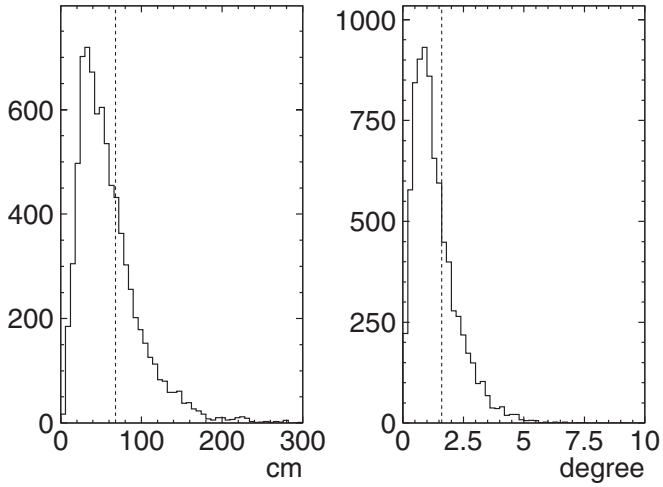

FIG. 16. Performance of the muon fitter. Left (right) figure shows the vertex (angular) correlation between generated and reconstructed Monte Carlo muon tracks. The area to the left of the dashed line in both plots shows the $1-\sigma$ (= 68%) included region.

V. CALIBRATION

A. Water transparancy measurement

Cherenkov photons can travel up to 60 m before reaching PMT's in Super-K, and so light attenuation and scattering in water directly affects the number of photons that are detected by the PMT's. Since the energy of an event is mainly determined from the number of hit PMT's, the water transparency (WT) must be precisely determined for an accurate energy measurement.

The water transparency in SK is monitored continuously by using the decay electrons (and positrons) from cosmic ray μ events that stop in the detector: $\mu^- \rightarrow e^- + \bar{\nu}_e + \nu_\mu$, and $\mu^+ \rightarrow e^+ + \nu_e + \bar{\nu}_\mu$. At SK's underground depth (2700 meter water equivalent), cosmic ray muons reach the detector at a rate of $\sim$2 Hz. Approximately 6000 μ's per day stop in the inner detector and produce a decay electron (or positron). In order to monitor the WT effectively, it is important to have a pure sample of electron events from muon decay (μ-e decay) events. Several criteria are applied to select these events:

(i) The time difference (ΔT) between the stopping μ event and the μ-e decay candidate must satisfy: 2.0 μ sec $<\Delta T <$ 8.0 μ sec .

(ii) The reconstructed vertex of the μ-e decay candidate must be contained within the 22.5 kton fiducial volume.

(iii) $N_{\rm hit}$ must be at least 50.

These criteria select $\sim$1500 μ-e decay events daily, which is sufficient statistics to search for variation in the WT in

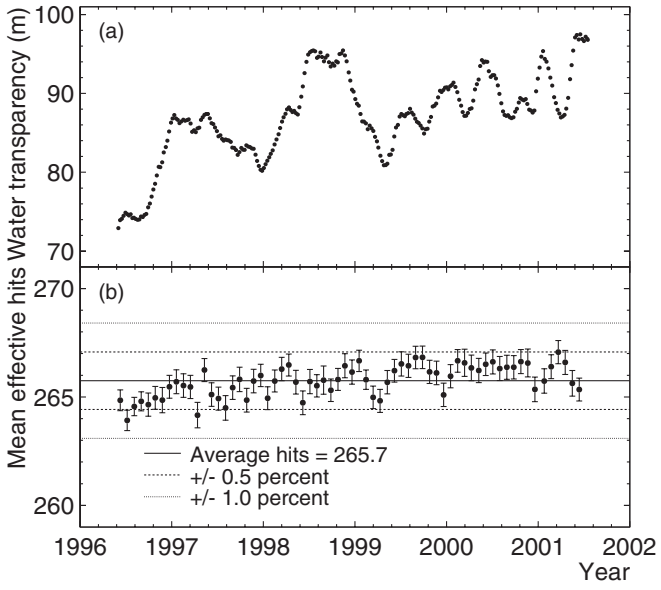

FIG. 17. (a) Time variation of the measured water transparency during SK-I. (b) Stability of the SK-I energy scale as a function of time. Each point represents the mean N_{eff} value for 28 days of μ_e decay events. The solid line represents the average N_{eff} for all μ_e decay events in SK-I; the dashed and dotted lines represent, respectively, $\pm 0.5\%$ and $\pm 1.0\%$ deviations from the average.

one week. The average energy of the μ-e decay events is $\sim$37 MeV, which is much higher than that of solar neutrinos (< 20 MeV). Therefore, the μ-e decays cannot be used for the absolute energy calibration. However, they can be used to monitor the stability of water transparency and energy scale over time.

In order to remove the effects of scattered and reflected light, hit PMT's are selected by the following criteria: (1) PMT's must have timing that falls within the 50 nsec timing window, after the time-of-flight subtraction, (2) PMT's must be within a cone of opening angle $32^\circ \sim 52^\circ$ with respect to the direction of the μ-e decay event. A plot of the number of hit PMT's vs distance from the vertex to the PMT is made using the selected PMT's, fit with a linear function, and the inverse of the slope gives the water transparency.

Figure 17(a) shows variations in the WT as a function of time. Each point on the plot represents WT for one week. In order to reduce the effects of statistical fluctuations on the weekly measurement, the WT for a given week is defined as a running average over five weeks of data. Figure 17(b) plots the mean N_{eff} value for μ-e decay events in SK-I. From this figure, it can be seen that the energy scale has remained stable to within $\pm 0.5\%$ during the SK-I runtime.

B. Energy calibration

The energy scale calibration is necessary to correctly convert the effective number of hits (N_{eff}) to the total energy of the recoil electrons induced by solar neutrinos. LINAC and DT calibration are discussed in this section.

1. LINAC

The primary instrument for energy calibration is an electron linear accelerator (LINAC). The LINAC calibration of Super-K has been discussed in detail elsewhere [9]. The LINAC is used to inject downward-going electrons of known energy and position into the SK tank. The momentum of these electrons is tunable, with a range of 5.08 MeV to 16.31 MeV; this corresponds well with the energies of interest to solar neutrino studies. LINAC data is collected at nine different positions in the SK tank, as shown in Fig. 18. The data are compared to MC, and MC is adjusted until its absolute energy scale agrees well with data in all the positions and momenta. Once adjusted, this MC is extrapolated to cover events in all directions throughout the entire detector.

The electrons are introduced into SK via a beam pipe whose endcap's exit window is a 100 μm-thick sheet of titanium. This allows electrons to pass through without significant momentum loss but prevents water from entering the beam pipe.

Seven different momentum data sets are taken at each LINAC position. The absolute energy in the LINAC system is measured with a germanium (Ge) detector. Table III shows the different momenta used in the LINAC calibration. The average occupancy at the beam pipe endcap is set to about 0.1 electrons/spill. The reason for this low occupancy is to reduce the number of spills which include multiple electrons.

The energy scale and resolution obtained by LINAC is compared to MC at each position and momentum.

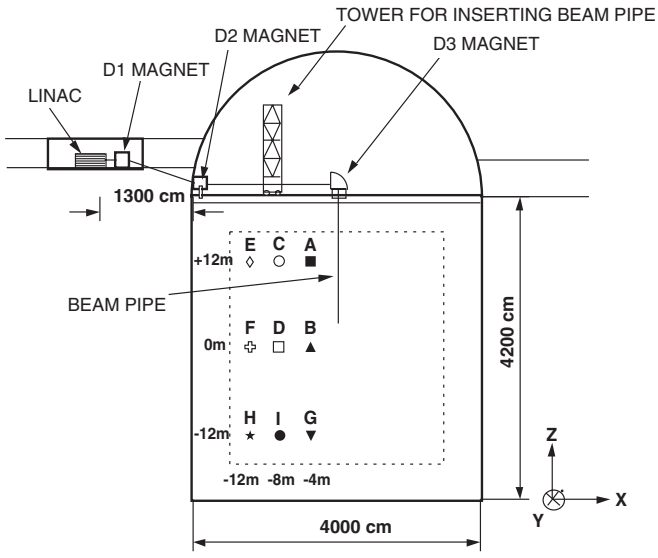

FIG. 18. The LINAC system at SK. The dotted line represents the fiducial volume of the detector and the letters (A to H) indicate the positions where LINAC data were taken.

TABLE III. LINAC beam momentum. The second column gives the energy measured in the Ge calibration system. The last column lists the total energy of the electrons after leaving the beam pipe, in which energy loss due to the 1 mm thick plastic scintillator used for triggering and the 0.1 mm thick titanium endcap window is taken into account.

Beam momentum (MeV/c)	Ge energy (MeV)	In-tank energy (MeV)
5.08	4.25	4.89
6.03	5.21	5.84
7.00	6.17	6.79
8.86	8.03	8.67
10.99	10.14	10.78
13.65	12.80	13.44
16.31	15.44	16.09

Figure 19(a) shows the deviation in the energy scale between data and MC. Figure 19(b) shows the average over all the positions from (a). The deviation at each position is less than 1% and the position averaged momentum dependence of the deviation is less than 0.5%.

Figure 20(a) shows the deviation of the energy resolution at each energy and position in LINAC calibration between data and MC, and 20(b) shows these deviations averaged over all positions. The difference in reconstructed energy resolution between data and MC is less than 2.5%.

The absolute energy scale of the detector was tuned by using the LINAC calibration data. The uncertainty of the absolute energy scale comes from the uncertainties of water transparency measurement when the LINAC calibration data was taken (0.22%), position dependence of the energy scale (0.21%), time variation of the energy scale obtained by LINAC calibration (0.11%), tuning accuracy

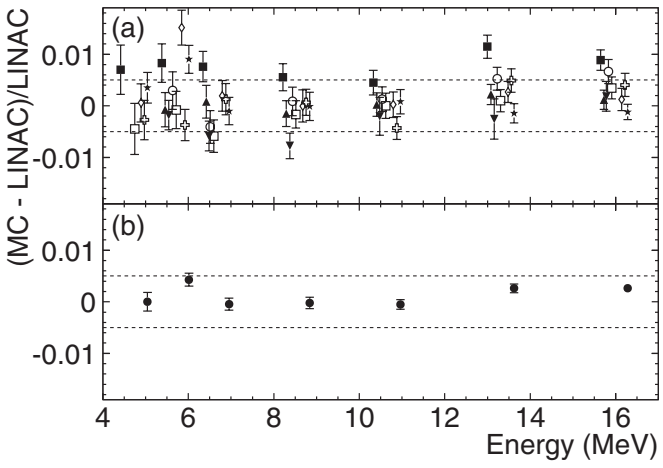

FIG. 19. The relative difference between the reconstructed energy of LINAC data and the corresponding MC. (a) The results are shown for all positions and beam momenta. (b) Averaged over all positions. The dashed lines show ±0.5%. See Fig. 18 for the positions.

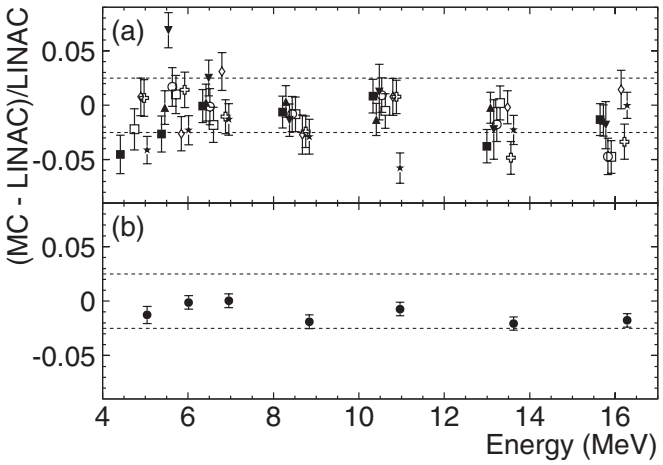

FIG. 20. The reconstructed energy resolution from LINAC data and MC. (a) shows the deviation of the resolution in each energy and position in LINAC calibration between data and MC; (b) averaged over all positions. The dashed lines show ±2.5%. See Fig. 18 for the positions.

of MC simulation (0.1%), electron beam energy determination in LINAC calibration (0.21%), and directional dependence of energy scale since the LINAC beam is only downward going (0.5%). Adding those contributions in quadrature, the total uncertainty of Super-K-I's absolute energy scale is estimated to be 0.64%.

2. ^{16}N *from the DT generator*

Even though the energy scale is determined from LINAC calibration and is fixed, ^{16}N also was used as a calibration source. Since events from ^{16}N decay are isotropic, they are useful in probing the directional dependence of the energy scale. Also, because of the portability of the DT generator we were able to probe the energy scale at many positions in the detector on a monthly basis.

With a half-life of 7.13 sec, the Q value of the decay of ^{16}N is 10.4 MeV, and the most probable decay mode produces a 6.1 MeV γ ray together with a β decay electron of maximum energy 4.3 MeV. Man-made ^{16}N was obtained using a deuterium-tritium neutron generator (''DT generator''). The DT generator uses the fusion reaction $^2\mathrm{H} + {}^3\mathrm{H} \rightarrow {}^4\mathrm{He} + n$ to produce 14.2 MeV neutrons. A fraction of the neutrons collide with ^{16}O to produce ^{16}N. The DT generator thus provided us with a large sample of essentially background free ^{16}N data for use in energy scale calibration. More details about the DT generator are given elsewhere [10].

The ^{16}N decay energy spectrum is a superposition of several γ ray lines and β continua of various end points. The reconstructed energy spectrum has a peak around $E_{\mathrm{peak}} = 6.9 \sim 7.0$ MeV. The shape of the peak region ($5.5 \sim 9.0$ MeV) is approximated by a Gaussian with a width of $1.6 \sim 1.7$ MeV. The deviation of this energy peak between data and MC is measured. Figure 21 shows 31

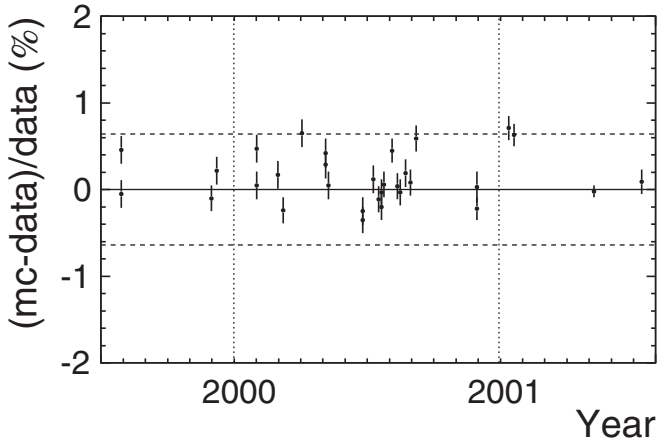

FIG. 21. The deviation between data and MC for the volume-averaged DT energy scale as a function of time. The DT generator was available for the last two years of SK-I, starting in July, 1999. The dashed line shows the $\pm 0.64\%$ of energy scale uncertainty, which is estimated by LINAC calibration as discussed in Sec. V B 1.

data sets of DT results during two years of running, and it shows the deviation is within $\pm 1\%$ when averaged over all positions.

The direction dependence of the energy scale is measured as follows. First, the deviation between data and MC is calculated for all directions. Then it is calculated for two divided data samples: events in the upward or downward directions. It should be noted that in all cases, the energy

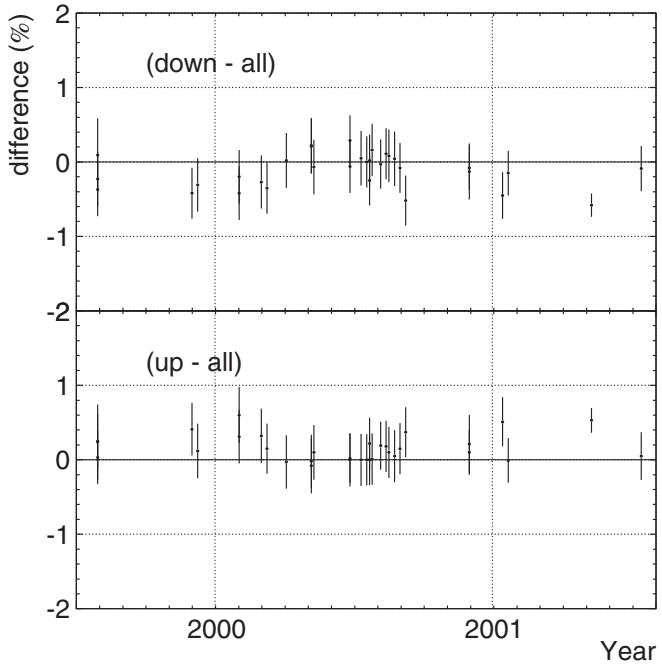

FIG. 22. Directional dependence of energy scale by DT calibration. Upper figure shows $R_{\mathrm{down}} - R$ as a function of time, lower figure shows the same for $R_{\mathrm{up}} - R$. Note that $R_{\mathrm{up}} \approx -R_{\mathrm{down}}$.

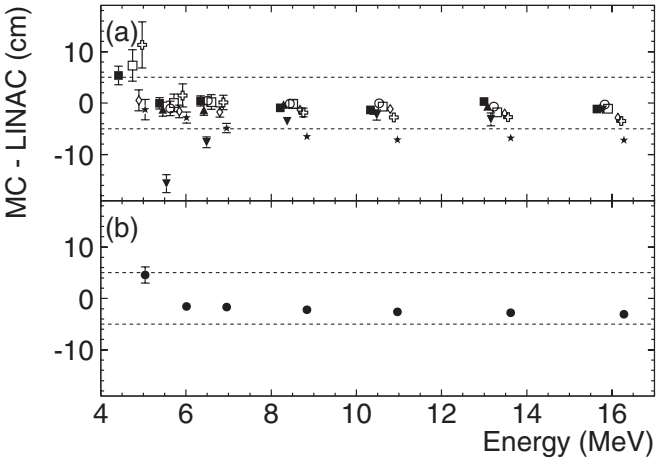

FIG. 23. The differences of vertex resolution between data and MC in LINAC. The dashed lines show ± 5 cm. (a) The deviation of the resolution in each position as a function of energy. The LINAC position symbols in this plot are defined in Fig. 18. (b) All the data are averaged over all positions.

scale is averaged over the detector volume. Figure 22 shows plots comparing the energy scale obtained from using just downward- or upward-going events to that determined by using the entire sample. The difference is within $\pm 0.6\%$.

C. Vertex calibration

Figure 23 shows the differences of the vertex resolution between data and MC in LINAC with several energies and positions. These differences are less than ± 5 cm.

The vertex shift in the reconstruction is estimated using a Ni(n, γ)Ni gamma source, [1] because the gamma ray is emitted in almost uniform directions. The vertex shift is

TABLE IV. The vertex shift measured by Ni(n, γ)Ni gamma source calibration. The unit is cm.

Position	Δx	Δy	Δz
(35.3, −70.7, −1200)	−1.8	−1.9	−2.8
(35.3, −70.7, 0)	0.6	−0.5	−2.8
(35.3, −70.7, +1200)	−1.1	−1.7	0.6
(35.3, −70.7, +1600)	0.0	−3.2	−3.5
(35.3, −1555.4, −1200)	−5.5	8.6	−9.1
(35.3, −1555.4, 0)	−5.5	23.4	−3.0
(35.3, −1555.4, +1200)	−0.5	7.0	6.0
(35.3, −1555.4, +1600)	−3.3	7.6	2.7
(35.3, −1201.9, −1200)	−4.2	5.4	−9.1
(35.3, −1201.9, 0)	−1.4	15.5	−2.2
(35.3, −1201.9, +1200)	2.5	8.9	4.2
(1520.0, −70.9, −1200)	−5.7	−1.4	−10.3
(1520.0, −70.9, 0)	−18.6	−3.0	−4.0
(1520.0, −70.9, +1200)	−12.6	−1.0	6.2
(−35.3, −1555.4, −1200)	3.7	−11.4	−8.6
(−35.3, −1555.4, 0)	6.6	−19.5	−2.0
(−35.3, −1555.4, +1200)	1.6	−20.3	7.2

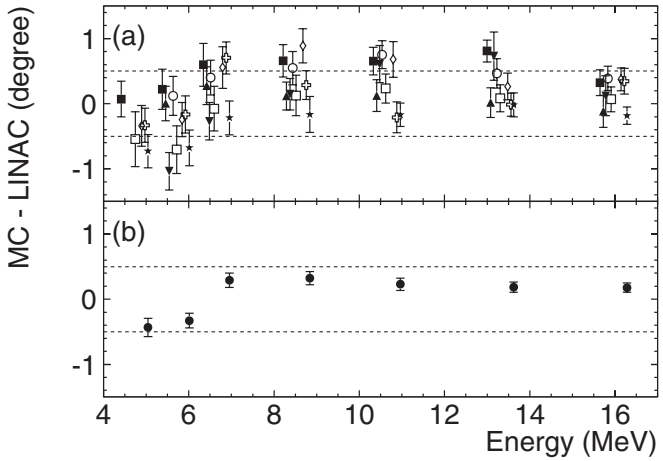

FIG. 24. The reconstructed angular resolution from LINAC data and MC. (a) shows the deviation of the resolution in each energy and position in LINAC calibration between data and MC. (b) is averaged over all positions. The dashed lines show ± 0.5 deg. See Fig. 18 for the positions.

defined as a vector from an averaged position of the reconstructed vertex of the data to that of a corresponding MC. Table IV shows the vertex shift at several source positions. The systematic error for the solar neutrino flux as a result of vertex shift (which could move events in or out of the fiducial volume) is evaluated from these values, and it is $\pm 1.3\%$.

D. Direction calibration

The angular resolution is calibrated by LINAC data and MC. Figure 24 shows the angular resolution variation in each energy and position between LINAC and Monte Carlo events. The difference in angular resolution between LINAC data and MC is less than $\pm 0.5°$.

We have applied this difference as a correction factor to the expected signal shape then taken the same amount of the correction as our systematic error due to angular resolution. This systematic error is 1.2%.

VI. BACKGROUND

A. Low energy backgrounds

The main background sources below about 6.5 MeV for the solar neutrino events are (1) events coming from outside fiducial volume, and (2) ^{222}Rn.

Figure 25 shows a typical vertex distribution of the low energy events before the Intelligent Trigger selection. Most of the low energy events occur near the inner detector's wall region. They originate from radioactivity of the PMT's, black sheet, PMT support structures, and mine rocks surrounding the SK detector. Though the fiducial volume is selected to be 2 m from this inner detector wall, there are a lot of remaining events around the edge of the fiducial volume. The reconstructed directions of these remaining, externally produced events in the fiducial volume are pointed, on average, strongly inward. We have eliminated most of these external events by using an event selection based upon vertex and direction information. The details of this event selection will be explained in Sec. VII D. Although most of these external events are eliminated by this cut, some quantity of external events still remain. These remaining external events are one of the major backgrounds in this energy region.

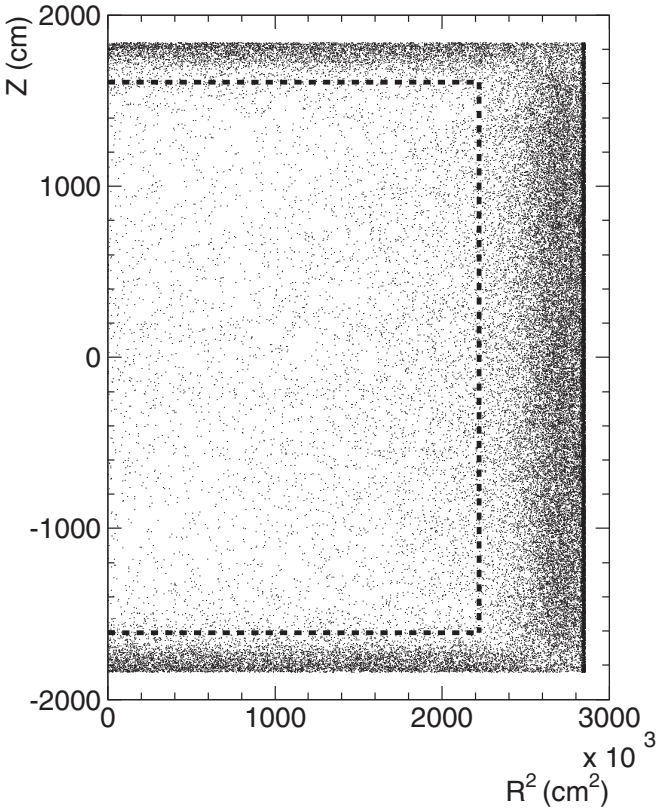

FIG. 25. Typical vertex distribution of the low energy events before the Intelligent Trigger selection. The analysis energy threshold for this plot is 5.0 MeV. The dashed line shows the fiducial volume edge.

Another major source of background in the low energy region are radioactive daughter particles from the decay of ^{222}Rn. ^{214}Bi, which is one of these daughter particles, undergoes beta decay with resulting electron energies up to 3.26 MeV. Because of the limited energy resolution of the detector, these electrons can be observed in this energy region.

We have reduced ^{222}Rn in the water by our water purification system to contribute less than 1 mBq/m^3 [1] and monitor the radon concentration in real-time by several radon detectors [11–13]. However, the water flow from the water inlets, located at the bottom of the SK detector, stirs radon emanated from the inner detector wall into the fiducial volume [14]. Therefore, there is an event excess after the external event cut in the detector bottom region as compared to the top region. We also supply radon-reduced

TABLE V. Possible radioactive spallation products in Super-Kamiokande.

Isotope	$\tau_{1/2}$ (sec)	Decay mode	Kinetic energy (MeV)
$^{8}_{2}$He	0.119	β^-	9.67 + 0.98 (γ)
		β^-n	(16%)
$^{8}_{3}$Li	0.838	β^-	$\sim$13
$^{8}_{5}$B	0.77	β^+	$\sim$13.9
$^{9}_{3}$Li	0.178	β^-	13.6 (50.5%)
		β^-n	($\sim$ 50%)
$^{9}_{6}$C	0.127	β^+p	3 $\sim$ 15
$^{11}_{3}$Li	0.0085	β^-	16 $\sim$ 20 ($\sim$ 50%)
		β^-n	$\sim$16 ($\sim$ 50%)
$^{11}_{4}$Be	13.8	β^-	11.51 (54.7%)
			9.41 + 2.1 (γ) (31.4%)
$^{12}_{4}$Be	0.0236	β^-	11.71
$^{12}_{5}$B	0.0202	β^-	13.37
$^{12}_{7}$N	0.0110	β^+	16.32
$^{13}_{5}$B	0.0174	β^-	13.44
$^{13}_{8}$O	0.0086	β^+	13.2, 16.7
$^{14}_{5}$B	0.0138	β^-	14.55 + 6.09 (γ)
$^{15}_{6}$C	2.449	β^-	9.77 (36.8%)
			4.47 + 5.30 (γ)
$^{16}_{6}$C	0.747	β^-n	$\sim$4
$^{16}_{7}$N	7.13	β^-	10.42 (28.0%)
			4.29 + 6.13 (γ) (66.2%)

air [14] into the space above the water surface in the SK tank to prevent radon in the mine air from dissolving into the purified water. The radon concentration in this radon-reduced air is less than 3 mBq/m^3 and the measured radon level in the air in the tank is stable at 20 $\sim$ 30 mBq/m^3. Periods of anomalously high radon concentration due to water system troubles were removed from this analysis.

B. High energy backgrounds

Above about 6.5 MeV, the dominant background source is radioactive isotopes produced by cosmic ray muons' spallation process with oxygen nuclei. Some fraction of downward-going cosmic ray muons interact with oxygen nuclei in the water and produce various radioactive isotopes. These radioisotopes are called ''spallation products.'' Table V shows a summary of possible spallation products in SK. The β and/or γ particles from the radioactive spallation products are observed in Super-K, causing what are called ''spallation events.'' The spallation events retain some correlation in time and space with their parent muons. Using this correlation, we have developed a cut to remove these spallation background events efficiently. The details of this cut will be explained in Sec. VII B.

VII. DATA ANALYSIS

A. Noise reduction

The first step of the data reduction is an elimination of the noise and obvious background events. First of all, the events with total photoelectrons less than 1000, which corresponds to $\sim$100 MeV, are selected. Next, the following data reductions are applied: (a) Events whose time difference since a previous event was less than 50 μ sec were removed in order to eliminate decay electrons from stopping muons. (b) Events with an outer detector trigger and over 20 outer PMT hits were removed in order to eliminate entering events like cosmic ray muons. (c) A function to categorize noise events is defined by the ratio of the number of hit PMT's with $|Q| \leq 1.0$ p.e. and the total number of hit PMT's. Since typical noise events should have many hits with low charge, events with this ratio larger than 0.4 were removed. (d) A function which can recognize an event where most of its hits are clustered in one electronics ADC-TDC module (ATM) is defined. It is the ratio of the maximum number of hits in any one module to the total number of channels (usually 12) in one ATM module. Events with a larger ratio than 0.95 were removed as they generally arose due to local radio frequency noise in one ATM module. (e) Events produced by flasher PMT's must be removed. These flasher events often have a relatively larger charge than normal events, therefore they are recognized using the maximum charge value and the number of hits around the maximum charge PMT. The slightly involved criterion is shown in Fig. 26. (f) An additional cut to remove noise and flasher events is applied using a combination of a tighter goodness cut (goodness $\leq$ 0.6)

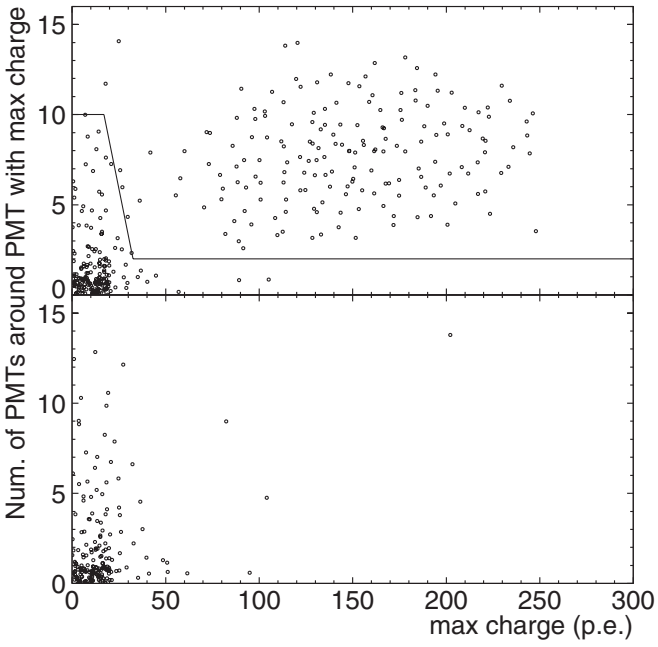

FIG. 26. The relation between max charge and the number of hit PMT's in a 5×5 patch surrounding the PMT with the maximum charge. At most 24 tubes in this patch (plus the one at the center) can be activated. The upper plot shows a typical distribution including active flasher events, and the lower plot shows a typical good data set. The cut region is the area above the line in the upper figure.

and a requirement of azimuthal uniformity in the Cherenkov ring pattern. Good events have a uniform azimuth distribution of hit PMT's along the reconstructed direction, while flasher events often have a cluster of hit PMT's which lead to a nonuniform azimuth distribution.

In this noise reduction, the number of candidate solar neutrino events went from 3.43×10^7 to 1.81×10^7 after applying the 2 m fiducial volume cut and constraining the energy region from 5.0 to 20.0 MeV. Table VII shows the reduction step summary.

The loss of solar neutrino signal by the noise reduction is evaluated to be 0.8% using a Ni(n, γ)Ni gamma source at several edge positions of the inner detector. The difference between data and MC for this source yields the systematic error for this series of reductions; it is $\pm 1.0\%$ for our solar neutrino flux measurement. The loss is mainly due to the flasher cut.

B. Spallation cut

The method to reject spallation products shown in Sec. VI is described in this section. In order to identify spallation events, likelihood functions are defined based on the following parameters:

(i) ΔL: Distance from a low energy event to the track of the preceding muon.
(ii) ΔT: Time difference from muon event to the low energy event.
(iii) $Q_{\rm res}$: Residual charge of the muon event, $Q_{\rm total} - Q_{\rm unit} \times L_\mu$, where $Q_{\rm total}$ is the total charge, $Q_{\rm unit}$ is the total charge per track length and L_μ is the reconstructed track length of the muon track.

Some fraction of muons deposit very large amounts of energy in the detector and in such cases vertex position reconstruction is not reliable. Therefore, the spallation likelihood functions are defined for the following two cases: in the case of a successful muon track fit,

$$L_{\rm spa}(\Delta L, \Delta T, Q_{\rm res}) = L_{\rm spa}^{\Delta L}(\Delta L, Q_{\rm res}) \times L_{\rm spa}^{\Delta T}(\Delta T) \times L_{\rm spa}^{Q_{\rm res}}(Q_{\rm res}), \quad (7.1)$$

in the case of a failure fit the muon track,

$$L_{\rm spa}(\Delta T, Q_{\rm total}) = L_{\rm spa}^{\Delta T}(\Delta T) \times L_{\rm spa}^{Q_{\rm total}}(Q_{\rm total}), \quad (7.2)$$

where $L_{\rm spa}^{\Delta L}(\Delta L, Q_{\rm res})$, $L_{\rm spa}^{\Delta T}(\Delta T)$, $L_{\rm spa}^{Q_{\rm res}}(Q_{\rm res})$, and $L_{\rm spa}^{Q_{\rm total}}(Q_{\rm total})$ are likelihood functions for ΔL, ΔT, and $Q_{\rm res}$.

Figure 27 shows the ΔL distributions from spallation candidates for six $Q_{\rm res}$ ranges, and the spallationlike function is made from these plots. Here, the selection criteria is $\Delta T < 0.1$ sec and $N_{\rm eff} \geq 50$ (equivalent to 7.2 MeV). The peak around $0 \sim 100$ cm is caused by spallation events and that around 1500 cm is due to chance coincidence. The distribution of nonspallation events is calculated using a sample which shuffles the event times randomly; it is the dashed line in the figure, and the nonspallationlike function is also made by these plots. After subtracting the nonspallation from the spallation function, and taking a ratio with a random coincidence distribution, $L_{\rm spa}^{\Delta L}(\Delta L, Q_{\rm res})$ was obtained.

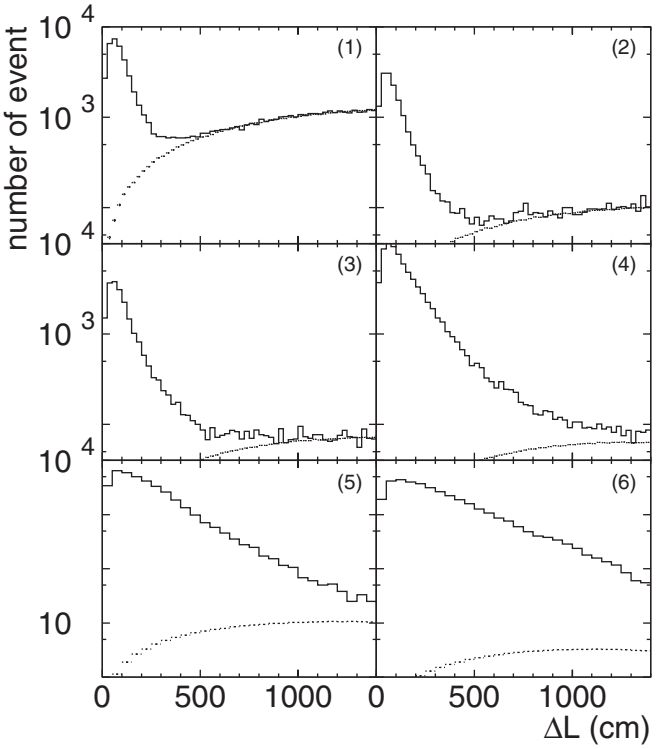

FIG. 27. ΔL distribution for each $Q_{\rm res}$ ranges, (1) $Q_{\rm res} < 2.4 \times 10^4$ p.e., (2) $2.4 \times 10^4 < Q_{\rm res} < 4.8 \times 10^4$ p.e., (3) $4.8 \times 10^4 < Q_{\rm res} < 9.7 \times 10^4$ p.e., (4) $9.7 \times 10^4 < Q_{\rm res} < 4.8 \times 10^5$ p.e., (5) $4.8 \times 10^5 < Q_{\rm res} < 9.7 \times 10^5$ p.e., (6) 9.7×10^5 p.e. $< Q_{\rm res}$. The solid line shows the data, and the dashed line shows the random sample.

Figure 28 shows the ΔT distributions from spallation candidates for each time range. Here, the selection criteria is $\Delta L < 300$ cm and $N_{\rm eff} \geq 50$ and $Q_{\rm res} < 10^6$ p.e.. These distributions are fitted with the following function:

$$L_{\rm spa}^{\Delta T}(\Delta T) = \sum_{i=1}^{7} A_i \left(\frac{1}{2}\right)^{-[(\Delta T)/\tau_{1/2}^i]}, \quad (7.3)$$

where $\tau_{1/2}^i$ are half-life times of typical radioactive elements produced by spallation and A_i's are fitting parameters. The evaluated half-life times and radioisotopes are summarized in Table VI. In order to obtain the likelihood function for residual charge $L_{\rm spa}^{Q_{\rm res}}(Q_{\rm res})$, time correlated events with low energy events ($\Delta T < 0.1$ sec, $N_{\rm eff} \geq 50$) and noncorrelated events are selected. Figure 29(a) shows the $Q_{\rm res}$ distribution for spallation and nonspallation candidates. After subtracting the nonspallation from the spallation function, the resulting distribution's fit by a polynomial function is shown in Fig. 29(b).

To employ the spallation cut, the likelihood values are calculated for all muons in the previous 100 sec before a low energy event, and a muon is selected which gives the

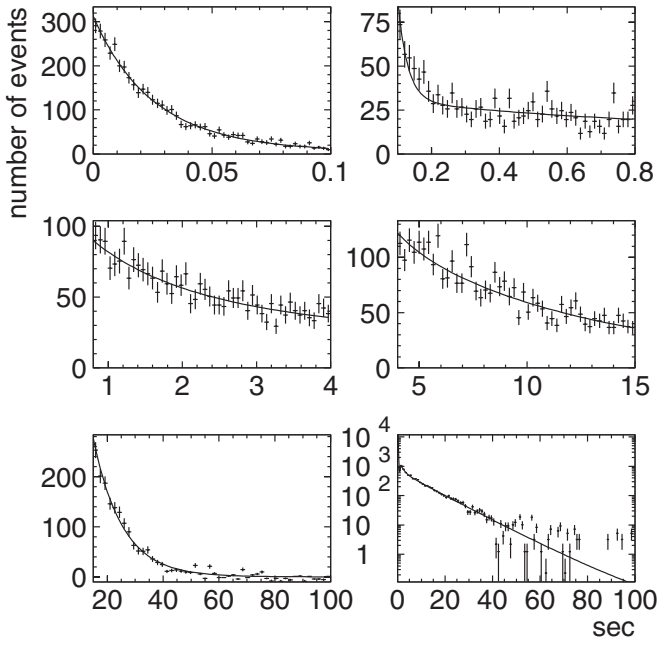

FIG. 28. ΔT distribution for each time range, (1) $0.0 < \Delta T < 0.1$ sec, (2) $0.1 < \Delta T < 0.8$ sec, (3) $0.8 < \Delta T < 4.0$ sec, (4) $4.0 < \Delta T < 15$ sec, (5) $15 < \Delta T < 100$ sec, (6) $0 < \Delta T < 100$ sec. Cross marks are data and lines are fitted likelihood function $L^{\Delta T}_{\rm spa}(\Delta T)$.

TABLE VI. The parameters of the likelihood $L^{\Delta T}_{\rm spa}(\Delta T)$.

i	Radioactivity	$\tau^i_{1/2}$	A_i
1	$^{12}_{5}$B	2.02×10^{-2}	1.20×10^{5}
2	$^{12}_{7}$N	1.10×10^{-2}	3.39×10^{4}
3	$^{9}_{3}$Li	1.78×10^{-1}	3.39×10^{2}
4	$^{8}_{3}$Li	8.40×10^{-1}	1.25×10^{3}
5	$^{15}_{6}$C	2.45	1.35×10^{2}
6	$^{16}_{7}$N	7.13	6.76×10^{2}
7	$^{11}_{4}$Be	13.83	7.79

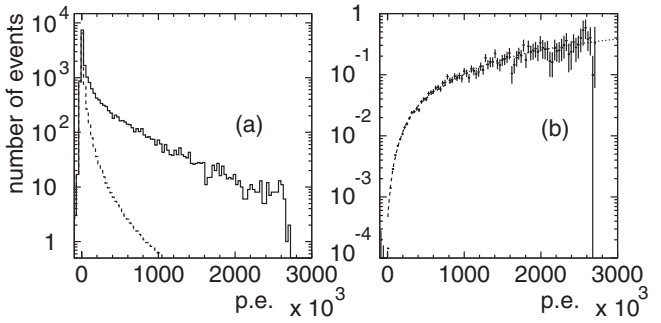

FIG. 29. (a) $Q_{\rm res}$ distribution for the spallation candidate events (solid line) and the noncandidate events (dashed line). (b) Cross marks show the result of subtracting dashed from solid line in (a), and dotted line shows the likelihood function $L^{Q_{\rm res}}_{\rm spa}(Q_{\rm res})$.

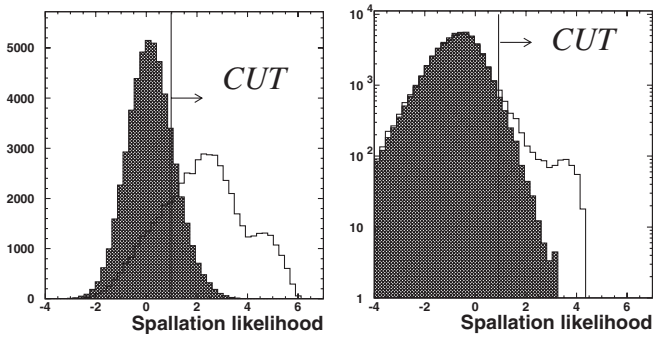

FIG. 30. The maximum likelihood value distribution for success [left figure, defined in Eq. (7.1)] and failure [right figure, defined in Eq. (7.2)] of muon track reconstruction. (See Sec. IV D for details.) The unshaded histogram shows all data while the hatched histogram shows the so-called random sample, in which the data is shuffled in time and position.

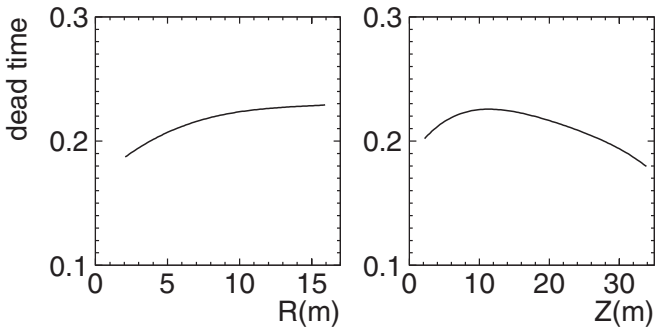

FIG. 31. Position dependence of the spallation cut's dead time. The horizontal axis shows the distance from the barrel (left), and the minimum distance from the top or bottom (right).

maximum likelihood value ($L_{\rm max}$). Figure 30 shows $L_{\rm max}$ distributions for both the successful muon track reconstruction case and the failed reconstruction case. To be considered a spallation event the selection criteria are $L_{\rm max} > 0.98$ (when fit succeeded) and $L_{\rm max} > 0.92$ (when fit failed).

The dead time for low energy events caused by the spallation cut is estimated to be 21.1%. This estimation is calculated using a low energy sample which is shuffled in time and position. It has some position dependence because of the SK tank geometry. Figure 31 shows the position dependence of the dead time as a function of the distance from the inner barrel wall and the top or bottom walls. The systematic error due to position dependence is estimated by comparing between MC and data, and it is estimated to be $\pm 0.2\%$ for flux and $\pm 0.1\%$ for day-night flux difference and other time variations.

C. Ambient background reduction

Even after the fiducial volume cut, some fraction of the ambient background still remains. It is mainly due to misreconstruction of the vertex position. In order to re-

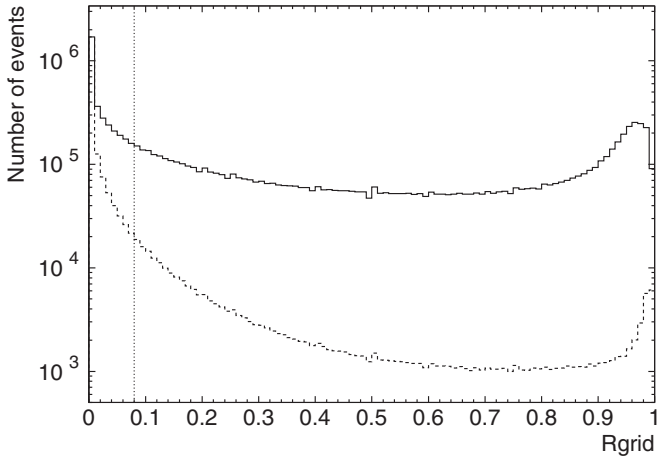

FIG. 32. R_{grid} distribution for data (solid line) and MC (dashed line). The normalization is done by scaling to the first bin. The dotted line shows the reduction criterion.

move the remaining background, several cuts to evaluate the quality of the reconstructed vertex were applied.

1. Fit stability cut.—The goodness value of the vertex was calculated for points in the region of the reconstructed vertex position and the sharpness of the goodness distribution as a function of detector coordinates was evaluated. First of all, the goodness at ~300 grid points around the original vertex are calculated, and their difference from the goodness at the reconstructed vertex (Δ_g) is determined. The number of test points which give a Δ_g more than some threshold was counted; the threshold is as a function of energy and vertex position. The ratio of the number of points over this threshold to the total number of grid points is defined as R_{grid}. The R_{grid} distribution of the data is shown in Fig. 32 along with simulated ^{8}B Monte Carlo events. Events with $R_{\mathrm{grid}} > 0.08$ are rejected as background. The systematic error of this reduction was evaluated using LINAC data and MC and the systematic error for flux measurement is estimated to be $\pm 1.0\%$.

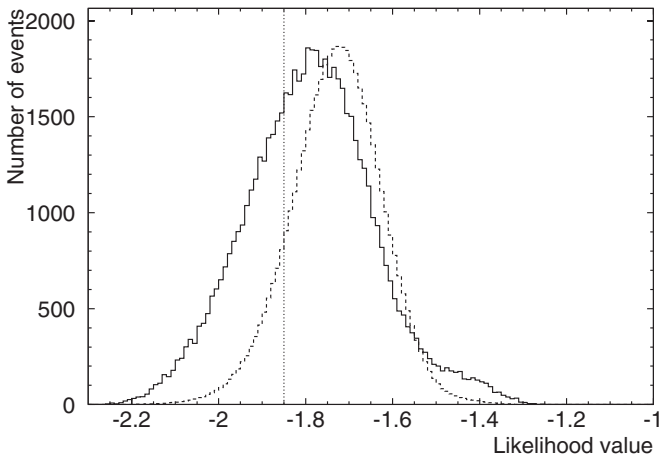

FIG. 33. The likelihood value distribution defined in Eq. (7.4) for data (solid line) and MC (dashed line). The dotted line shows the reduction criteria. Events with a likelihood of less than -1.85 are rejected.

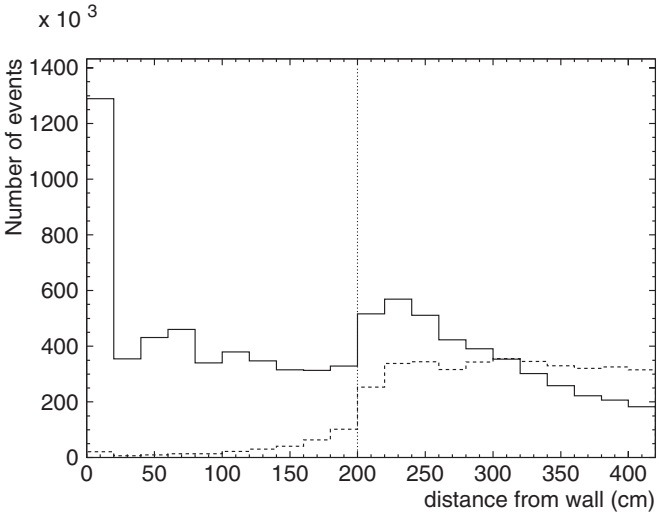

FIG. 34. The distance from the wall distribution using the second vertex reconstruction for data (solid line) and MC (dashed line). The normalization of MC is done by the total number of events. The dotted line shows the reduction criteria.

2. Hit pattern cut.—Misreconstructed events often do not have the expected Cherenkov ring pattern when the hit PMT's are viewed from the reconstructed vertex. Also, some fraction of spallation products like ^{16}N emit multiple gammas in addition to an electron and so do not fit a single Cherenkov ring pattern very well. In order to remove those kind of events, the following likelihood function is defined:

TABLE VII. The summary of number of events remaining after each reduction step.

Total	3.43×10^7
A.	Noise reduction
(a)	2.66×10^7
(b)	2.51×10^7
(c)	2.50×10^7
(d)	2.50×10^7
(e)	2.48×10^7
(f)	1.81×10^7
B.	Spallation cut
	1.29×10^7
C.	Ambient B. G. cut
(a)	3.61×10^6
(b)	2.72×10^6
(c)	1.86×10^6
D.	Gamma cut
	2.96×10^5
E.	^{16}N cut
	2.87×10^5

$$L(E,\vec{x}) \equiv \frac{\sum_{i=1}^{N_{\rm hit}} \log(f(\cos\theta_{\rm dir}, E, \vec{x}))_i}{N_{\rm hit}}. \qquad (7.4)$$

Here, $f(\cos\theta_{\rm dir}E,\vec{x})$ is the same function as that derived from MC in Eq. (4.3), but here it depends on energy and vertex position. Figure 33 shows the likelihood distribution Eq. (7.4) for data and ^{8}B MC. The events with a likelihood less than -1.85 are rejected. The systematic error of this cut is estimated using solar neutrino MC and a sample of very short lived spallation products; it is $+1.0\%$ and -0.5% for the flux measurement.

3. Fiducial volume cut using the second vertex fitter.— The 2 m fiducial volume cut using the second vertex reconstruction described in Sec. IVA is applied. Figure 34 shows the distance from the wall distribution of data and MC using the second vertex reconstruction. Table VII also shows the reduction step summary described in this section.

D. Gamma ray cut

The gamma ray cut is used for reduction of external gamma rays which mainly come from the surrounding rock, PMT glass, and stainless steel support structure of the detector. These gamma rays are one of the major background especially for solar neutrino data.

The distinctive feature of external gamma rays is that they travel from the outside edge of the SK volume and continue on to the inside. In order to remove this kind of event, reconstructed direction and vertex information is used to define the effective distance from the wall, $d_{\rm eff}$, as shown in the inset of the left plot in Fig. 35. As they emanate from the wall itself, the value $d_{\rm eff}$ for external gamma ray events should be small. Figure 35 also shows $d_{\rm eff}$ distributions for data and MC. The criterion of the gamma ray cut is determined by maximizing its significance; here the number of remaining events after reduction in data and MC are used to define the significance, $N_{\rm MC}/\sqrt{N_{\rm data}}$. The gamma ray cut criteria are determined to be

(1) $d_{\rm eff} \geq 450$ cm (for $E \geq 6.5$ MeV);
(2) $d_{\rm eff} \geq 800$ cm (for 5.0 MeV $\leq E < 6.5$ MeV).

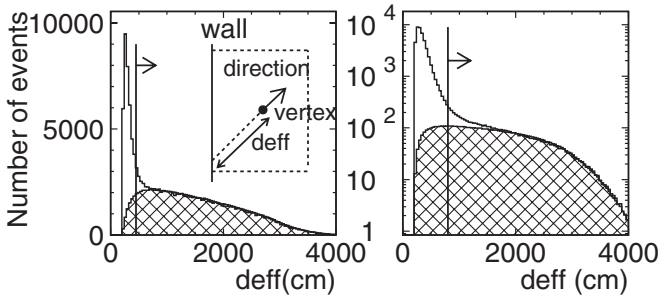

FIG. 35. Effective distance ($d_{\rm eff}$) of $E \geq 6.5$ MeV (left) and 5.0 MeV $\leq E < 6.5$ MeV (right). Blank histogram shows data and hatched area shows solar neutrino MC.

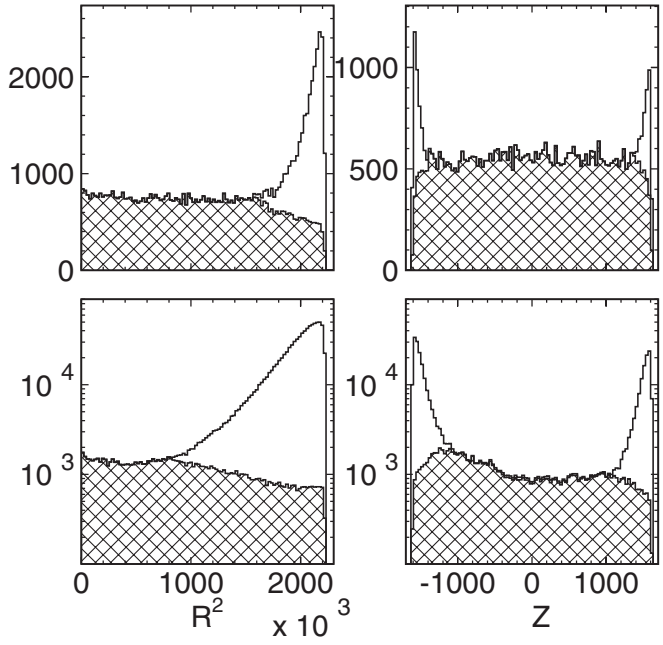

FIG. 36. Vertex distribution before (blank) and after (hatched) applying the gamma ray cut. The left plots are R^2 for $|Z| <$ 1000 cm, and the right ones are Z for $|R| <$ 1000 cm. The upper plots show $E \geq 6.5$ MeV, and lower ones show 5.0 MeV $\leq E <$ 6.5 MeV.

Figures 36 and 37 show the vertex and direction distributions before and after the gamma ray cut for real data in the energy regions $E \geq 6.5$ MeV and 5.0 MeV $\leq E < 6.5$ MeV. The inefficiencies introduced by this cut in the energy regions $E \geq 6.5$ MeV and 5.0 MeV $\leq E <$ 6.5 MeV are estimated to be 6.9% and 22.0%.

Since the gamma ray cut uses reconstructed vertex and direction, the differences of vertex and angular resolution between data and MC can introduce systematic errors. In order to estimate this effect, we shift the reconstructed vertex and direction of events within the difference of

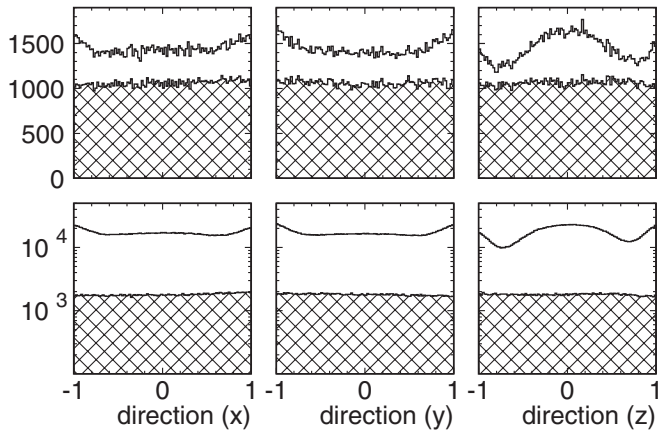

FIG. 37. Directional distribution (x, y, z) before (blank) and after (hatched) applying the gamma ray cut. The upper plots show $E \geq 6.5$ MeV, and the lower plots show 5.0 MeV $\leq E <$ 6.5 MeV.

data and MC, which are measured by LINAC, and apply the gamma ray cut to these events. The difference of reduction efficiency before and after this shift is taken to be the systematic error for the gamma ray cut. The systematic error of this cut for the flux measurement is estimated to be $\pm 0.5\%$, while for the energy spectrum it is estimated to be $\pm 0.1\%$.

E. ^{16}N cut

^{16}N background is generated by the capture of μ^- on ^{16}O nucleus in water:

$$^{16}\mathrm{O} + \mu^- \rightarrow {}^{16}\mathrm{N} + \nu_\mu.$$

The most probable decay mode of ^{16}N produces a 6.1 MeV γ ray together with a β decay electron of maximum energy 4.3 MeV; its half-life is 7.13 sec.

To tag this kind of event, spatial and time correlations with captured stopping muons are used. The selection method is as follows: (1) in order to select only a captured muon sample, collect a sample of stopping muons which are not followed by a decay event in 100 μ sec, then (2) select a low energy event sample within 335 cm from the stopping point of the muon as well as in a time window of 100 msec to 30 sec following the stopping muon. The number of such candidate low energy events is 9843 in 1496 days of low energy data. The inefficiency for this reduction is estimated by using a so-called random sample, where the time and vertex positions of the events have been mixed randomly. The same ^{16}N event selection as described above is then applied to the random sample, yielding an inefficiency for the ^{16}N cut of 0.49%.

F. Event reduction summary

Figure 38 shows the reduction efficiencies after each step as a function of energy using MC simulation events. The efficiency is used as a correction when the energy spectrum is calculated as described in Sec. VIII D.

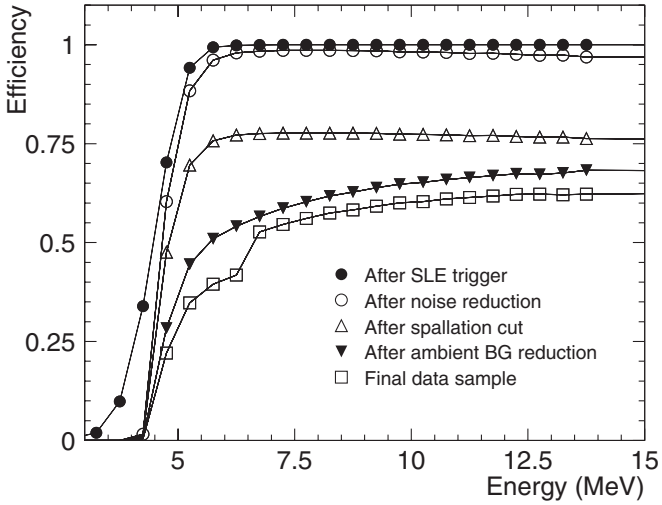

FIG. 38. Summary of the reduction efficiencies on MC.

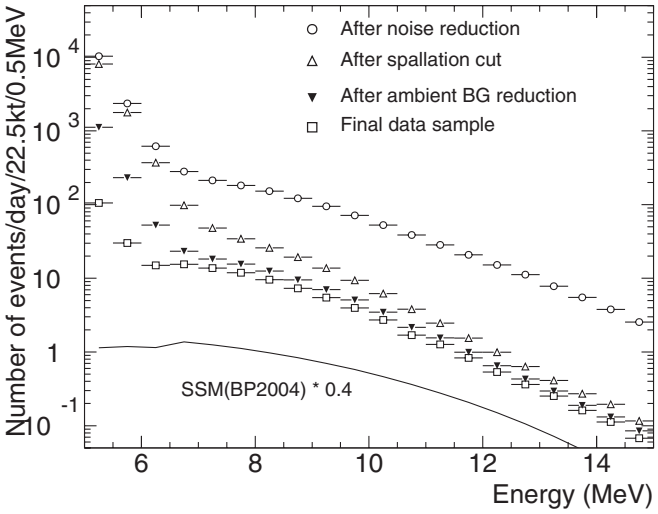

FIG. 39. Summary of the data reduction steps.

Figure 39 shows the event rate after each reduction step for data and also shows the predicted solar neutrino spectrum. Table VII summarizes the numerical results of the reduction steps. The number of events after all the reduction steps is 286 557.

VIII. RESULTS

A. Solar neutrino signal extraction

The solar neutrino signal is extracted from the directional correlation of the recoiling electrons with the incident neutrinos in ν-e scattering. Figure 40 shows $\cos\theta_{\mathrm{sun}}$ where θ_{sun} is the angle between the reconstructed recoil electron direction and the expected neutrino direction (calculated from the position of the sun at the event time).

The solar neutrino flux is extracted by a likelihood fit of the solar neutrino signal and the background to this distribution. This likelihood function is defined as follows:

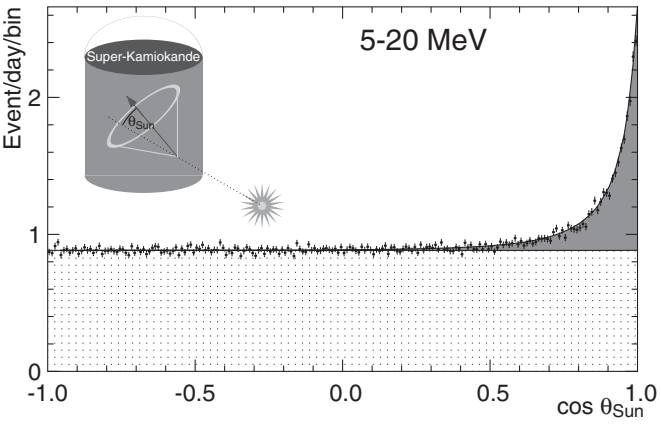

FIG. 40. Angular distribution of solar neutrino event candidates. The shaded area indicates the elastic scattering peak. The dotted area is the contribution from background events.

$$\mathcal{L} = e^{-(\sum_i B_i + S)} \prod_{i=1}^{N_{\rm bin}} \prod_{j=1}^{n_i} (B_i \cdot b_{ij} + S \cdot Y_i \cdot s_{ij}). \quad (8.1)$$

We define $N_{\rm bin} = 21$ energy bins: 18 energy bins of 0.5 MeV between 5.0 and 14.0 MeV, two energy bins of 1 MeV between 14.0 and 16.0 MeV, and one bin between 16.0 and 20.0 MeV. S is the total number of solar neutrino signal events, and n_i, B_i, and Y_i represent the number of observed events, the number of background events, and the expected fraction of signal events in the ith energy bin, respectively. We use two types of probability density functions: $p(\cos\theta_{\rm sun}, E)$ describes the angular shape expected for solar ν_e's of recoil electron energy E (signal events) and $u_i(\cos\theta_{\rm sun})$ is the background shape in energy bin i. Each of the n_i events in energy bin i is assigned the background factor $b_{ij} = u_i(\cos\theta_{ij})$ and the signal factor $s_{ij} = p(\cos\theta_{ij}, E_j)$.

The signal shape $p(\cos\theta_{\rm sun}, E)$ is obtained from the known, strongly forward-peaked angular distribution of neutrino-electron elastic scattering with smearing due to multiple scattering and the detector's angular resolution. The background shape $u_i(\cos\theta_{\rm sun})$ has no directional correlation with the neutrino direction, but deviates from a flat shape due to the cylindrical shape of the SK detector: the number of PMT's per solid angle depends on the SK zenith angle. In order to calculate the expected background shape, we use the angular distribution of data itself. The presence of solar neutrinos in the sample biases mostly the azimuthal distribution, so at first we fit only the zenith angle distribution and assume the azimuthal distribution to be flat. We generate toy Monte Carlo directions according to this fit and calculate $\cos\theta_{\rm sun}$. We also fit both zenith and azimuthal distributions, approximately subtracting the solar neutrino events from the sample and repeat the toy Monte Carlo calculation. We compare the obtained number of solar neutrino events from both background shapes and assign the difference as a systematic uncertainty. Since the azimuthal distributions do not deviate very significantly from flat distributions, we quote the solar neutrino events obtained from the first shape (assuming a flat azimuthal distribution). The dotted area in Fig. 40 shows this background shape. The systematic uncertainty due to the background shape is 0.1% for the entire data sample (5.0–20.0 MeV). If the data sample is divided into a day and a night sample, the systematic uncertainty is 0.4%. The amount of background contamination is much less above 10 MeV than it is near the SK-I energy threshold (5.0 MeV), so small differences in background shape between the two methods become important only in the lowest energy bins: between 5.0 and 5.5 MeV, the systematic uncertainty is estimated to be 1.2%, between 5.5 and 6.0 MeV 0.4%, and above 6.0 MeV 0.15%.

TABLE VIII. Systematic error of each item (in %).

	Flux	Seasonal	Day-night
Energy scale, resolution	± 1.6	$^{+1.2}_{-1.1}$	$^{+1.2}_{-1.1}$
Theoretical uncertainty for ^{8}B spectrum	$^{+1.1}_{-1.0}$		
Trigger efficiency	$^{+0.4}_{-0.3}$	± 0.1	
Reduction	$^{+2.1}_{-1.6}$	± 0.5	
Spallation dead time	± 0.2	± 0.1	± 0.1
Gamma ray cut	± 0.5	± 0.25	
Vertex shift	± 1.3		
Background shape for signal extraction	± 0.1		± 0.4
Angular resolution	± 1.2		
Cross section of ν-e scattering	± 0.5		
Livetime calculation[a]	± 0.1	± 0.1	± 0.1
Total	$^{+3.5}_{-3.2}$	± 0.3	$^{+1.3}_{-1.2}$

[a]Caused by the event rate-dependent timing accuracy of our main data acquisition computer.

B. Observed solar neutrino flux

Figure 40 shows the $\cos\theta_{\rm sun}$ distribution for 1496 days of SK-I data. The best-fit value for the number of signal events due to solar neutrinos between 5.0 MeV and 20.0 MeV is calculated by the maximum likelihood method in Eq. (8.1), and the result for SK-I is $22\,404 \pm 226({\rm stat})^{+784}_{-717}({\rm sys})$. The corresponding ^{8}B flux is

$$2.35 \pm 0.02({\rm stat}) \pm 0.08({\rm sys}) \times 10^6 \ {\rm cm}^{-2}\,{\rm s}^{-1}.$$

The systematic errors for the solar neutrino flux, seasonal variation, and day-night differences for the energy range 5.0 MeV to 20.0 MeV are shown in Table VIII. The detailed explanations are written in each topic's section, but the total systematic error for the solar neutrino flux measurement is estimated to be $^{+3.5\%}_{-3.2\%}$.

C. Time variations of solar neutrino flux

1. Day-night difference

The day time flux and night time flux of solar neutrinos in SK-I are calculated using events which occurred when the solar zenith angle cosine was less than and greater than zero, respectively. The observed fluxes are

$$\Phi_{\rm day} = 2.32 \pm 0.03({\rm stat})^{+0.08}_{-0.07}({\rm sys}) \times 10^6 \ {\rm cm}^{-2}\,{\rm s}^{-1},$$

$$\Phi_{\rm night} = 2.37 \pm 0.03({\rm stat})^{+0.08}_{-0.08}({\rm sys}) \times 10^6 \ {\rm cm}^{-2}\,{\rm s}^{-1}.$$

Their difference leads to a day-night asymmetry, defined as $\mathcal{A} = (\Phi_{\rm day} - \Phi_{\rm night})/(\frac{1}{2}(\Phi_{\rm day} + \Phi_{\rm night}))$. We find

$$\mathcal{A} = -0.021 \pm 0.020({\rm stat})^{+0.013}_{-0.012}({\rm sys}).$$

Including systematic errors, this is less than $1-\sigma$ from zero asymmetry. The largest sources of systematic error in the asymmetry are energy scale and resolution ($^{+0.012}_{-0.011}$) and

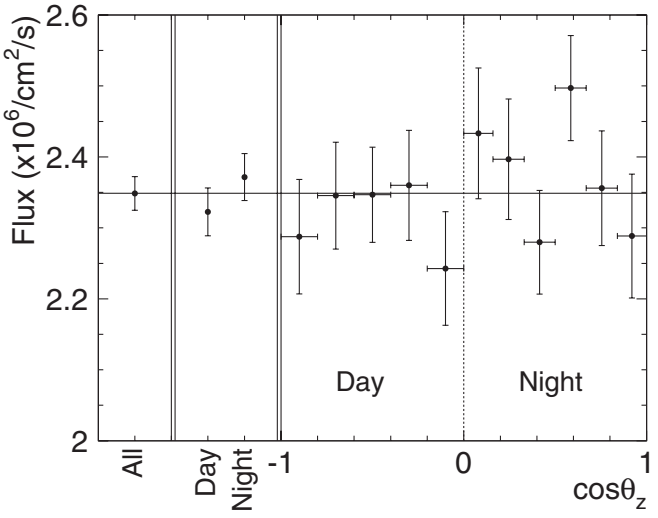

FIG. 41. The solar zenith angle dependence of the solar neutrino flux (error bars show statistical error). The width of the night time bins was chosen to separate solar neutrinos that pass through the Earth's dense core (the rightmost Night bin) from those that pass through the mantle. The horizontal line shows the flux for all data.

the nonflat background shape of the $\cos\theta_{\rm sun}$ distribution (± 0.004). As described in the neutrino oscillation analysis section, we can reduce the statistical uncertainty if we assume two-neutrino oscillations within the large mixing angle region. The day-night asymmetry in that case is

$$\mathcal{A} = -0.017 \pm 0.016(\text{stat})^{+0.013}_{-0.012}(\text{sys}) \pm 0.0004(\text{osc})$$

with the final, tiny additional uncertainty due to the uncertainty of the oscillation parameters themselves. Figure 41 shows the solar neutrino flux as a function of the solar zenith angle cosine.

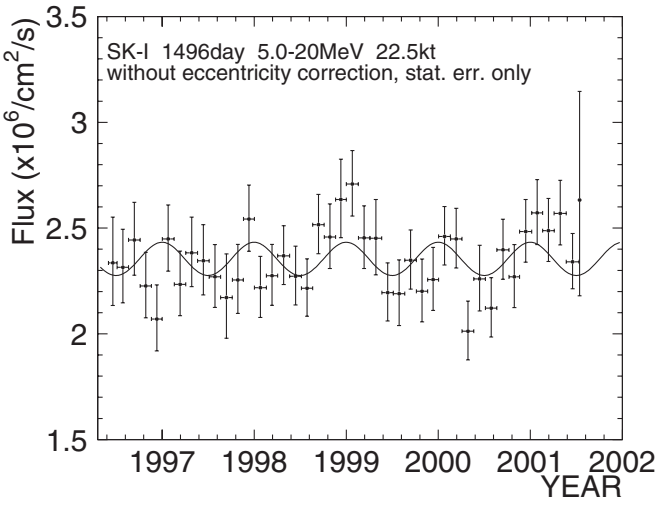

FIG. 42. Solar neutrino flux as a function of time. The binning of the horizontal axis is 1.5 months. The curve shows the expected flux time variance. The wavy shape comes from the eccentricity in the Earth's orbit around the Sun.

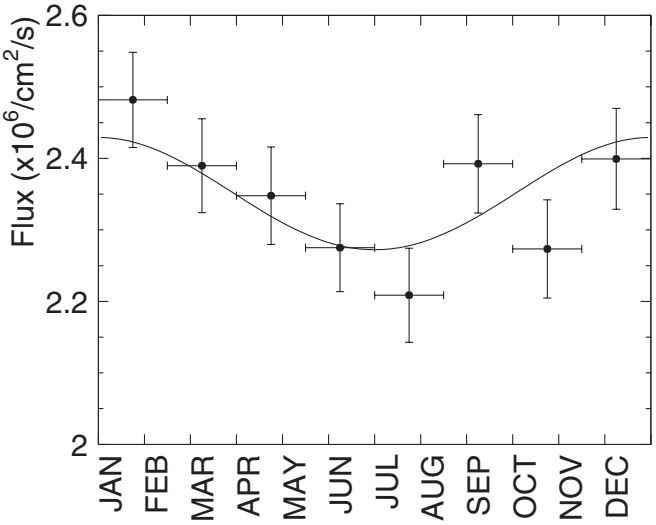

FIG. 43. The seasonal variation of the solar neutrino flux. The solid line is the prediction based on the eccentricity of the Earth's orbit.

2. Seasonal variation

Figure 42 shows the monthly variation of the flux, which each horizontal bin covers 1.5 months. The figure shows that the experimental operation is very stable.

Figure 43 shows the seasonal variation of solar neutrino flux. As in Fig. 42, each horizontal time bin is 1.5 months wide, but in this figure data taken at similar times during the year over the entire course of SK-I's data taking has been combined into single bins. The 1.7% orbital eccentricity of the Earth, which causes about a 7% flux variation simply due to the inverse square law, is included in the flux prediction (solid line). The observed flux variation is consistent with the predicted annual modulation. Its χ^2/d.o.f. is 4.7/7, which is equivalent to 69% C.L. If we fit the eccentricity to the Earth's orbit to the observed SK rate variation, the perihelion shift is 13 ± 18 days (with respect to the true perihelion) and the eccentricity is $2.1 \pm 0.3\%$ [15]. This is the world's first observation of the eccentricity of the Earth's orbit made with neutrinos. The total systematic error on the relative flux values in each seasonal bin is estimated to $\pm 1.3\%$. The largest sources come from energy scale and resolution ($^{+1.2\%}_{-1.1\%}$) and reduction cut efficiency ($\pm 0.5\%$), as shown in Table VIII.

D. Energy spectrum

Figure 44 shows the expected and measured recoil electron energy spectrum. The expected spectrum is calculated by the detector simulation described in Sec. III, and BP2004 is used as a solar model. The solid line shows the expected spectrum of ^{8}B and hep neutrinos, and the dashed line shows the contribution of only ^{8}B neutrinos.

The observed and expected event rates are summarized in Tables IX and X. The values in these tables are corrected by the reduction efficiencies listed in Fig. 38.

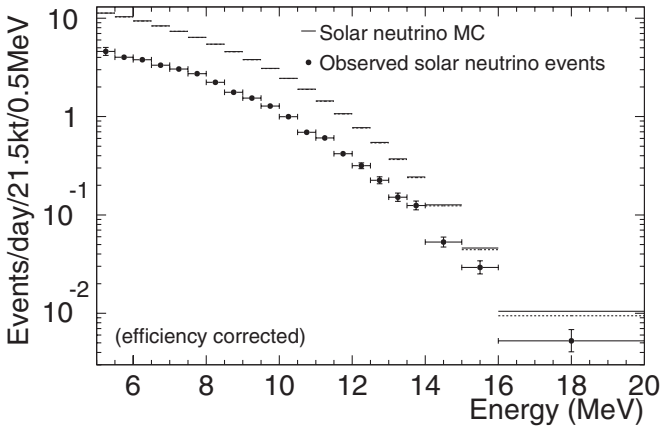

FIG. 44. Energy spectrum of the solar neutrino signal. The horizontal axis is the total energy of the recoil electrons. The vertical axis is the event rate of the observed solar neutrino signal events. The error bars are a quadrature of the statistical and uncorrelated errors. The reduction efficiencies in Fig. 38 are corrected. BP2004 SSM flux values are used for the ^{8}B and hep MC fluxes in this plot. The dashed line shows the contribution of only ^{8}B.

The uncorrelated and correlated systematic errors for each energy bin are shown in Tables XI and XII, respectively.

E. Hep solar neutrino

The expected hep neutrino flux is 3 orders of magnitude smaller than the ^{8}B solar neutrino flux. However, since the end point of the hep neutrino spectrum is about 18.8 MeV compared to about 16 MeV for the ^{8}B neutrinos, the high energy end of the ^{8}B spectrum should be relatively enriched with hep neutrinos. In order to discuss the flux of hep neutrinos, the most sensitive energy region for hep neutrino was estimated, then, assuming all the signal events in this energy region were due to hep neutrinos, an upper limit of the hep solar neutrino flux was obtained. Any possible effects from neutrino oscillations were not considered in this analysis.

Figure 45 shows the expected integral energy distributions for solar neutrinos. In the high energy region, the relative hep contribution is high, but the expected number of events is small because of the limited observation time. For this analysis, the best energy aperture for the hep solar

TABLE IX. Observed and expected event rates in each energy bin at 1 AU. The unit of the rates is events/kton/year. The errors in the observed rates are statistical only. All the values are corrected by the reduction efficiencies in Fig. 38. The expected event rates are for the BP2004 SSM flux values (^{8}B flux is 5.79×10^6, hep flux is $7.88 \times 10^3/\mathrm{cm}^2/\mathrm{sec}$). θ_z is the angle between the z axis of the detector and the vector from the Sun to the detector.

Energy (MeV)	Observed rate All $-1 \le \cos\theta_z \le 1$	Day $-1 \le \cos\theta_z \le 0$	Night $0 < \cos\theta_z \le 1$	Expected rate ^{8}B	hep
5.0–5.5	$74.7^{+6.6}_{-6.5}$	$72.1^{+9.5}_{-9.4}$	$77.1^{+9.2}_{-9.0}$	182.9	0.312
5.5–6.0	$65.0^{+3.3}_{-3.2}$	$64.8^{+4.7}_{-4.6}$	$65.1^{+4.6}_{-4.5}$	167.7	0.309
6.0–6.5	$61.5^{+2.4}_{-2.3}$	$60.2^{+3.4}_{-3.3}$	$62.6^{+3.3}_{-3.2}$	151.9	0.294
6.5–7.0	$54.1^{+1.7}_{-1.7}$	$54.2^{+2.4}_{-2.4}$	$53.9^{+2.4}_{-2.3}$	135.3	0.284
7.0–7.5	$49.4^{+1.5}_{-1.5}$	$49.2^{+2.2}_{-2.1}$	$49.6^{+2.1}_{-2.1}$	119.2	0.266
7.5–8.0	$44.3^{+1.4}_{-1.4}$	$44.8^{+2.0}_{-1.9}$	$43.8^{+1.9}_{-1.9}$	103.5	0.249
8.0–8.5	$36.3^{+1.2}_{-1.2}$	$35.7^{+1.7}_{-1.7}$	$36.8^{+1.7}_{-1.7}$	88.3	0.236
8.5–9.0	$28.7^{+1.0}_{-1.0}$	$26.6^{+1.5}_{-1.4}$	$30.6^{+1.5}_{-1.4}$	74.1	0.221
9.0–9.5	$25.0^{+0.9}_{-0.9}$	$25.4^{+1.4}_{-1.3}$	$24.6^{+1.3}_{-1.2}$	61.4	0.196
9.5–10.0	$20.8^{+0.8}_{-0.8}$	$20.7^{+1.2}_{-1.1}$	$20.8^{+1.2}_{-1.1}$	49.9	0.185
10.0–10.5	$16.2^{+0.7}_{-0.7}$	$15.7^{+1.0}_{-0.9}$	$16.7^{+1.0}_{-0.9}$	39.6	0.167
10.5–11.0	$11.2^{+0.6}_{-0.5}$	$10.9^{+0.8}_{-0.7}$	$11.5^{+0.8}_{-0.8}$	30.7	0.149
11.0–11.5	$9.85^{+0.51}_{-0.49}$	$9.65^{+0.74}_{-0.68}$	$10.03^{+0.73}_{-0.68}$	23.28	0.130
11.5–12.0	$6.79^{+0.42}_{-0.40}$	$7.14^{+0.63}_{-0.58}$	$6.47^{+0.58}_{-0.53}$	17.27	0.118
12.0–12.5	$5.13^{+0.36}_{-0.33}$	$5.05^{+0.52}_{-0.47}$	$5.21^{+0.51}_{-0.46}$	12.45	0.098
12.5–13.0	$3.65^{+0.30}_{-0.28}$	$3.96^{+0.46}_{-0.41}$	$3.38^{+0.41}_{-0.36}$	8.76	0.090
13.0–13.5	$2.46^{+0.25}_{-0.23}$	$2.56^{+0.38}_{-0.33}$	$2.37^{+0.35}_{-0.30}$	5.94	0.073
13.5–14.0	$2.02^{+0.22}_{-0.20}$	$1.95^{+0.32}_{-0.27}$	$2.09^{+0.32}_{-0.27}$	3.88	0.060
14.0–15.0	$1.72^{+0.21}_{-0.19}$	$1.60^{+0.31}_{-0.25}$	$1.85^{+0.31}_{-0.26}$	4.01	0.094
15.0–16.0	$0.949^{+0.157}_{-0.133}$	$0.750^{+0.218}_{-0.165}$	$1.136^{+0.238}_{-0.192}$	1.439	0.057
16.0–20.0	$0.341^{+0.103}_{-0.077}$	$0.240^{+0.148}_{-0.093}$	$0.423^{+0.156}_{-0.109}$	0.611	0.068

TABLE X. Observed and expected event rates in each zenith-spectra data set at a 1 AU distance from the Sun. The unit of the rates is events/kton/year. The errors in the observed rates are statistical only. All the values are corrected by the reduction efficiencies in Fig. 38. The expected event rates are for the BP2004 SSM flux values. θ_z is the angle between the z axis of the detector and the vector from the Sun to the detector.

Energy (MeV)	Observed rate							Expected rate	
	Day $\cos\theta_z$: $-1 \sim 0$	Mantle1 $0 \sim 0.16$	Mantle2 $0.16 \sim 0.33$	Mantle3 $0.33 \sim 0.50$	Mantle4 $0.50 \sim 0.67$	Mantle5 $0.67 \sim 0.84$	Core $0.84 \sim 1$	^{8}B	hep
5.5–6.5	$127.^{+6.}_{-6.}$	$124.^{+15.}_{-15.}$	$106.^{+14.}_{-14.}$	$132.^{+13.}_{-12.}$	$146.^{+13.}_{-12.}$	$140.^{+14.}_{-13.}$	$119.^{+15.}_{-14.}$	320.	0.603
6.5–8.0	$149.^{+4.}_{-4.}$	$166.^{+11.}_{-10.}$	$158.^{+10.}_{-9.}$	$137.^{+8.}_{-8.}$	$150.^{+8.}_{-8.}$	$141.^{+9.}_{-9.}$	$137.^{+10.}_{-9.}$	358.	0.799
8.0–9.5	$87.8^{+2.6}_{-2.6}$	$90.7^{+7.2}_{-6.8}$	$92.1^{+6.7}_{-6.4}$	$90.5^{+5.8}_{-5.5}$	$99.8^{+5.9}_{-5.6}$	$90.3^{+6.4}_{-6.0}$	$88.5^{+7.0}_{-6.6}$	223.8	0.653
9.5–11.5	$57.1^{+1.9}_{-1.8}$	$56.5^{+5.2}_{-4.8}$	$63.3^{+5.0}_{-4.6}$	$56.8^{+4.1}_{-3.9}$	$59.6^{+4.2}_{-3.9}$	$60.1^{+4.6}_{-4.3}$	$60.9^{+5.2}_{-4.8}$	143.4	0.631
11.5–13.5	$18.7^{+1.0}_{-0.9}$	$20.0^{+2.8}_{-2.4}$	$13.8^{+2.3}_{-2.0}$	$15.3^{+2.0}_{-1.8}$	$19.5^{+2.2}_{-2.0}$	$17.0^{+2.3}_{-2.0}$	$20.4^{+2.7}_{-2.3}$	44.4	0.379
13.5–16.0	$4.28^{+0.48}_{-0.43}$	$4.78^{+1.45}_{-1.08}$	$6.97^{+1.56}_{-1.24}$	$5.82^{+1.22}_{-0.98}$	$5.58^{+1.19}_{-0.95}$	$3.70^{+1.14}_{-0.85}$	$3.93^{+1.27}_{-0.93}$	9.33	0.211

TABLE XI. Energy-uncorrelated systematic errors for each energy bin.

Energy (MeV)	5–5.5	5.5–6	6–6.5	6.5–7	7–
Trigger efficiency	$^{+2.5}_{-1.5}$	$^{+0.8}_{-0.6}$	±0.1	±0.2	
Reduction	±0.9	±0.9	±0.9	±0.9	±0.9
Gamma ray cut	±0.1	±0.1	±0.1	±0.1	±0.1
Vertex shift	±0.2	±0.2	±0.2	±0.2	±0.2
Background shape for signal extraction	±0.6	±0.5	±0.1	±0.1	±0.1
Angular resolution	±2.3	±1.0	±1.0	±1.0	±1.0
Cross section of ν-e attering	±0.2	±0.2	±0.2	±0.2	±0.2
Total	$^{+3.5}_{-29}$	$^{+1.7}_{-1.6}$	±1.4	±1.5	±1.4

TABLE XII. Energy-correlated systematic errors for each of the 21 energy bins.

Energy	Scale (%)		Resolution (%)		Theory (%)	
5.0–5.5	+0.1	0.0	+0.2	−0.2	+0.1	0.0
5.5–6.0	−0.1	+0.1	+0.2	−0.2	0.0	+0.1
6.0–6.5	−0.3	+0.2	+0.2	−0.2	−0.1	+0.1
6.5–7.0	−0.5	+0.4	+0.2	−0.2	−0.3	+0.2
7.0–7.5	−0.7	+0.6	+0.2	−0.2	−0.4	+0.4
7.5–8.0	−0.9	+0.9	+0.2	−0.2	−0.5	+0.5
8.0–8.5	−1.1	+1.1	+0.2	−0.2	−0.7	+0.7
8.5–9.0	−1.4	+1.4	+0.1	−0.1	−0.9	+0.9
9.0–9.5	−1.7	+1.8	+0.1	−0.1	−1.1	+1.1
9.5–10.0	−1.9	+2.1	0.0	0.0	−1.3	+1.4
10.0–10.5	−2.3	+2.5	−0.1	+0.1	−1.5	+1.7
10.5–11.0	−2.6	+2.8	−0.3	+0.2	−1.8	+2.0
11.0–11.5	−3.0	+3.2	−0.5	+0.4	−2.1	+2.3
11.5–12.0	−3.4	+3.6	−0.8	+0.7	−2.4	+2.6
12.0–12.5	−3.8	+4.1	−1.1	+0.9	−2.7	+3.0
12.5–13.0	−4.3	+4.5	−1.4	+1.3	−3.1	+3.3
13.0–13.5	−4.8	+5.0	−1.9	+1.7	−3.4	+3.8
13.5–14.0	−5.4	+5.5	−2.4	+2.2	−3.8	+4.2
14.0–15.0	−6.3	+6.3	−3.3	+3.1	−4.4	+5.0
15.0–16.0	−7.7	+7.6	−4.9	+4.7	−5.1	+6.2
16.0–20.0	−9.9	+10.2	−8.1	+8.2	−5.6	+8.7

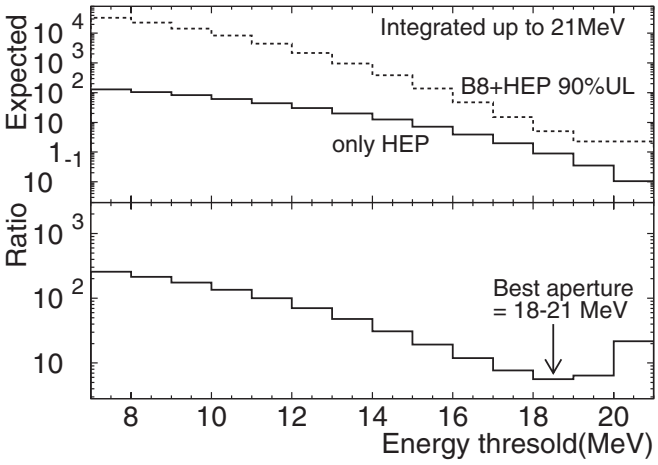

FIG. 45. Integral energy distributions for the hep solar neutrino analysis. The horizontal axis is the energy threshold of the recoil electrons. The integration is up to 21.0 MeV. Upper plot: the vertical axis is the expected number of events in SK-I's 1496 day final data sample after all cuts. The solid and dashed lines correspond to the hep solar neutrino only and the ^{8}B + hep 90% C.L. upper limit. Lower plot: the ratio of the two histograms in the upper plot (dashed line/solid line).

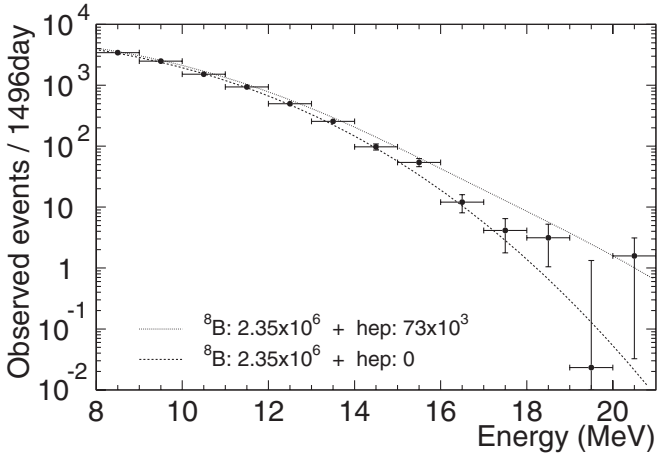

FIG. 46. Energy spectrum of recoil electrons in the high energy region. The points show data with statistical error bars. The curves show expected spectra with various hep contributions to the best-fit ^{8}B spectrum. The unit of the fluxes for the curves are $/\mathrm{cm}^2/\mathrm{s}$. The dotted and dashed curves show the spectrum with 73 and 0 ($\times 10^3/\mathrm{cm}^2/\mathrm{s}$) hep fluxes, respectively.

neutrinos was determined to be $18.0 \sim 21.0$ MeV. In this energy region 0.90 hep solar neutrino events are expected from the predicted BP2004 standard solar model (SSM) rate.

Applying the same signal extraction method to the data events in the $18.0 \sim 21.0$ MeV region, we found 4.9 ± 2.7 solar neutrino signal events. Assuming that all of these events are due to hep neutrinos, the 90% confidence level upper limit of the hep neutrino flux was $73 \times 10^3\ \mathrm{cm}^{-2}\,\mathrm{s}^{-1}$. Figure 46 shows the differential energy spectrum of solar neutrino signals in the high energy region.

IX. SOLAR NEUTRINO OSCILLATION ANALYSIS

A. Introduction

Two-neutrino oscillations are so far sufficient to explain and describe all measured solar neutrino phenomena. The flavor eigenstates ν_e and ν_x (where ν_x is either ν_μ or ν_τ or an admixture of both) describe weak interactions of neutrinos and electrons or nucleons. Only solar ν_e's can participate in charged-current reactions, since the solar neutrino energy is below the μ mass threshold. These flavor eigenstates are related to the mass eigenstates ν_1 and ν_2 via the unitary mixing matrix U, which for two neutrinos can be expressed in terms of a single parameter, the weak mixing angle θ:

$$U = \begin{pmatrix} \cos\theta & \sin\theta \\ -\sin\theta & \cos\theta \end{pmatrix}.$$

In vacuum, the neutrino wave function oscillates in space with a frequency of $\sqrt{p^2 + m^2} \approx p + m^2/2p$ leading to an oscillatory transition probability of the flavor eigenstates

$$p_{e\to x} = p_{x\to e} = \sin^2 2\theta \sin^2\left(\pi \frac{L}{L_{\mathrm{osc}}}\right), \qquad (9.1)$$

where the oscillation length $L_{\mathrm{osc}} = \frac{\pi}{1.27}\frac{E}{\Delta m^2}$. In a medium of matter density ρ, the small angle scattering of the ν_e flavor differs (due to the additional charged-current amplitude) from the ν_x flavor; this can be described with a matter potential $\Delta V(\rho)$. The transition probability is still given by Eq. (9.1) but with the "effective" oscillation length and mixing angle

$$L_{\mathrm{eff}} = \frac{\pi}{1.27\sqrt{(2\Delta V + \frac{\Delta m^2}{E}\cos 2\theta)^2 + (\frac{\Delta m^2}{E}\sin 2\theta)^2}},$$

$$\tan 2\theta_{\mathrm{eff}} = \frac{\frac{\Delta m^2}{E}\sin 2\theta}{2\Delta V + \frac{\Delta m^2}{E}\cos 2\theta}.$$

These relations are valid only for a constant matter potential (and therefore constant matter density). We calculate the oscillation probability by means of a numerical simulation using the position-dependent matter density profile in the Sun and Earth (shown in Fig. 47).

As noted by Mikheyev, Smirnov, and Wolfenstein (MSW) [16], the matter density in the Sun (see Fig. 47) is large enough for a resonance ($\Delta V = -\frac{\Delta m^2}{2E}\cos 2\theta$) to occur, producing effective maximal mixing ($\theta_{\mathrm{eff}} = \frac{\pi}{4}$) even if the fundamental mixing θ is small. The solar and terrestrial matter densities influence the transition probability for solar neutrinos between $\Delta m^2/E \approx 10^{-9}\ \mathrm{eV}^2/\mathrm{MeV}$ and $\approx 10^{-5}\ \mathrm{eV}^2/\mathrm{MeV}$ (MSW range).

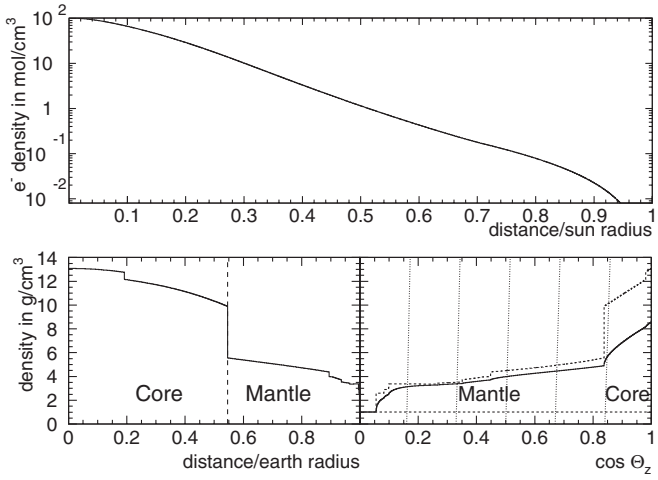

FIG. 47. The Sun's electron density profile from the standard solar model [7] (SSM) as a function of the distance to the center (top panel), and Earth's mass density profile (bottom panels). The left plot shows the density as a function of the distance to the Earth's center. The right plot shows the minimum (dashed horizontal line), average (solid line), and maximum density (dashed line) a solar neutrino of zenith angle θ_z encounters on its path through the Earth. The electron density is obtained from this by multiplying by $0.497\ \mathrm{mol/cm}^3$ for the mantle and $0.468\ \mathrm{mol/cm}^3$ for the core.

For the so-called large mixing angle (LMA: $\theta \approx \pi/6$) MSW "solution" to the solar neutrino problem, Δm^2 is chosen so that the solar neutrino spectrum lies at the "end" of this range (near 10^{-5} eV^2/MeV). It explains all observed solar neutrino interaction rates. In the case of the small mixing angle (SMA: $\theta \approx 0.05$) MSW solution, which also explains all observed rates, the solar neutrino spectrum must be placed near 10^{-7} eV^2/MeV (closer to the center of the MSW range). Other large angle solutions exist as well: the low Δm^2 solution (LOW) lies near the "beginning" of the MSW range (10^{-8} eV^2/MeV), while the (quasi-) vacuum (VAC) solutions are "below" the MSW range (10^{-12} eV^2/MeV to 10^{-11} eV^2/MeV).

To calculate the solar neutrino interaction rate on Earth, three steps are required: (i) the probability p_1 (p_2) of a solar neutrino, which is born as ν_e in the core of the Sun, to emerge at the surface as ν_1 (ν_2), (ii) coherent or incoherent propagation of the ν_1, ν_2 admixture to the surface of the Earth, (iii) the probability p_{1e} (p_{2e}) for a ν_1 (ν_2) neutrino to appear as ν_e in the detector (after propagation through part of the Earth, if the Sun is below the horizon, using the PREM [17] density profile of the Earth as shown in Fig. 47). In and above the MSW range of $\Delta m^2/E$, the distance between the Sun and the Earth is much larger than the vacuum oscillation length, so the propagation (ii) can be assumed to be incoherent. In that case, the total survival probability of the ν_e flavor is

$$p_e = p_1 \times p_{1e} + p_2 \times p_{2e} = 2p_1 p_{1e} + 1 - p_1 - p_{1e},$$

where p_1 and p_{1e} are computed numerically. Below the MSW range, both the solar and terrestrial matter densities can be neglected. However, the distance L between the Sun and the Earth approaches the oscillation length, so (ii) must be done coherently, and the survival probability of the ν_e flavor is

$$p_e = 1 - p_{e\to x} = 1 - \sin^2 2\theta \sin^2\left(\pi \frac{L}{L_{\rm osc}}\right)$$

using Eq. (9.1). Figure 48 shows (as an example) the survival probability of ^{8}B neutrinos. Other solar neutrino branches may have slightly different probabilities, because the radial distributions of the neutrino production location differ.

Neutrino oscillations impact SK data in three independent ways: (i) Since electron neutrinos have a much larger elastic scattering cross section than other flavors, neutrino oscillations reduce the rate of solar neutrino interactions. (ii) The spectrum of recoil electrons is distorted due to the energy dependence of the survival probability. (iii) The influence of the Earth's matter on the survival probability induces an apparent time dependence of the solar neutrino interaction rate with a 24-hour period. The amplitude of

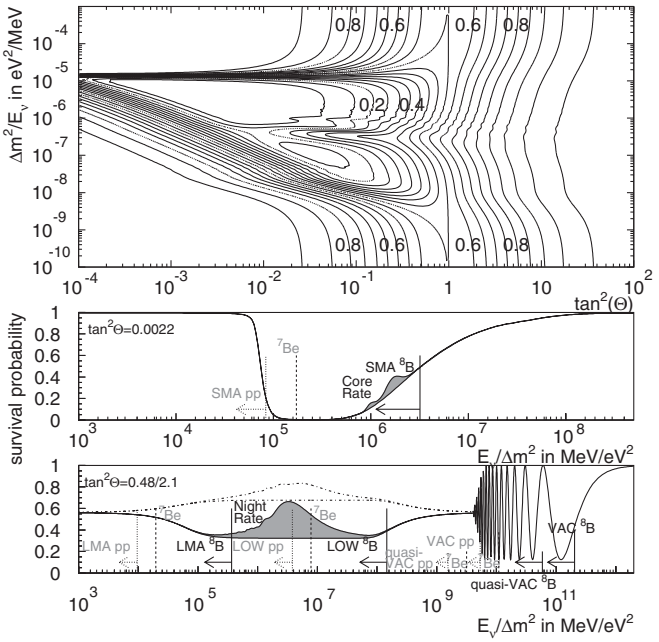

FIG. 48. Survival probability for ^{8}B solar neutrinos. The top plot displays contours of equal probability as a function of $\Delta m^2/E$ and $\tan^2\theta$. The middle panel shows the same probability as a function of $\Delta E/m^2$ only where a particular (small) mixing angle has been selected. The shaded area contrasts the difference between neutrinos passing through the core of the Earth (which has the highest matter density) with neutrinos arriving directly from the Sun. The bottom panel shows a large mixing case. The line above the shaded area depicts the average probability for neutrinos passing through the Earth. Superimposed on these two lower panels are the locations of three neutrino branches (pp-dotted, ^{7}Be-dashed, and ^{8}B-solid) for the SMA, LMA, LOW, VAC, and quasi-VAC solutions.

that time dependence is expressed in the day/night asymmetry $\frac{D-N}{0.5(D+N)}$ where D (N) is the averaged interaction rate during the day (night). Because of the eccentricity of the Earth's orbit, the distance between Sun and Earth changes periodically. Since the survival probability depends on this distance (if the neutrinos propagate coherently), this leads to another time variation (with a 365-day period) expressed in the summer/winter asymmetry $\frac{S-W}{0.5(S+W)}$ where S (W) is the averaged interaction rate during the summer (winter), corrected for the $1/r^2$ dependence of the solar neutrino intensity. The day/night and summer/winter variations cannot both be present in the SK data, since above a Δm^2 of about 10^{-8} eV^2 neutrinos propagate incoherently and below 10^{-8} eV^2 the Earth's matter effects on the survival probability are negligible. Figure 49 depicts the expected SK day/night asymmetry and Fig. 50 the summer/winter asymmetry, depending on the oscillation parameters. They also show the SK sensitivity to distortions of the recoil electron spectrum.

Using the survival probability p_e, the neutrino interaction rate due to the neutrino spectrum $I(E_\nu)$ at SK is

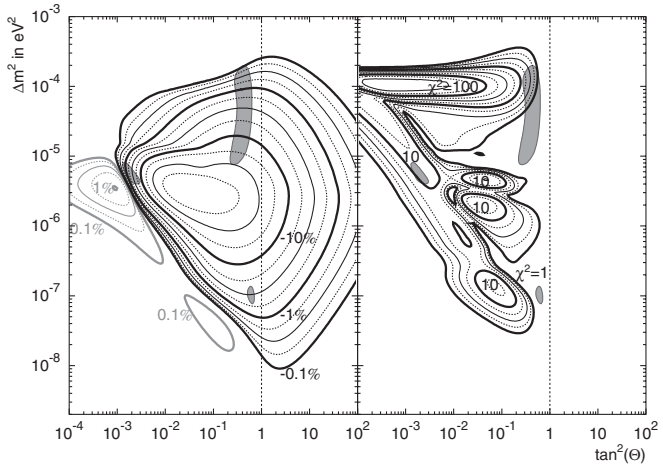

FIG. 49. Expected SK day/night asymmetry (left) and spectral distortion (right) in the MSW region. The scale of the contours of equal asymmetry (distortion) is logarithmic. The spectral distortion is measured in terms of a χ^2 using the SK spectrum uncertainties (but not the values of the SK spectrum). The gray shaded areas correspond to the LMA, SMA, and LOW solutions.

$$r_{\rm osc} = \int_{E_0}^{E_1} dE \int_{E_\nu} dE_\nu I(E_\nu) \int_{E_e} dE_e R(E_e, E) \times (S_e(E_\nu, E_e)p_e + S_x(E_\nu, E_e)(1 - p_e)),$$

where $S_{e,x}(E_\nu, E_e)$ describe the probability that the elastic scattering of a $\nu_{e,x}$ of energy E_ν with electrons produces a recoil electron of energy E_e. The Super-Kamiokande detector response is given by $R(E_e, E)$, which describes the probability that a recoil electron of energy E_e is reconstructed with energy E. The rate $r = r_{\rm noosc}$ expected without oscillation is obtained by setting p_e to 1. Since p_e is different for each neutrino species (pp, ^{8}B, *hep*, etc.), the calculation must be repeated for each relevant species. Because of its recoil electron energy threshold of 5.0 MeV, Super-Kamiokande-I is only sensitive to ^{8}B and hep neutrinos. The oscillation analysis was performed by two methods: the first method subdivides the data sample in both recoil electron energy and solar zenith angle (zenith spectrum), while the second method uses only energy bins and searches for time variations by means of an unbinned likelihood (unbinned time variation).

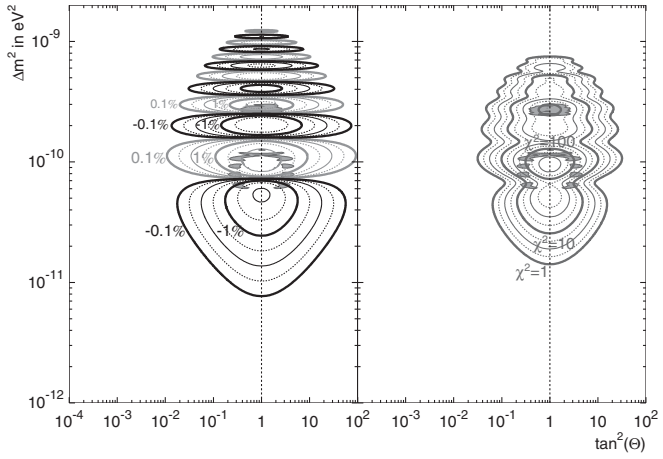

FIG. 50. Expected SK summer/winter asymmetry (left) and spectral distortion (right) in the vacuum oscillation region. The scale of the contours of equal asymmetry (distortion) is logarithmic. The spectral distortion is measured in terms of a χ^2 using the SK spectrum uncertainties (but not the values of the SK spectrum). The gray shaded areas correspond to the VAC solutions.

B. Analysis of the zenith spectrum χ^2

If $B^{\rm osc}_{i,z}$ ($H^{\rm osc}_{i,z}$) denote the expected ^{8}B (hep) neutrino induced rate in energy bin i and zenith angle bin z and $D_{i,z}$ the measured rate, the quantities b, h, and d are defined as follows:

$$b_{i,z} = \frac{B^{\rm osc}_{i,z}}{B_{i,z} + H_{i,z}},$$

$$h_{i,z} = \frac{H^{\rm osc}_{i,z}}{B_{i,z} + H_{i,z}}, \quad \text{and} \quad d_{i,z} = \frac{D_{i,z}}{B_{i,z} + H_{i,z}}.$$

For d, the rate calculations in the denominator use a full Monte Carlo simulation of the Super-Kamiokande detector. Figure 51 shows the average d in 21 and 8 energy bins. In Fig. 52, the individual $d_{i,z}$ are shown for 6 solar zenith angle bins. Now all zenith angle bins are combined into vectors. The rate difference vector

$$\vec{\Delta}_i(\beta, \eta) = (\beta \cdot \vec{b}_i + \eta \cdot \vec{h}_i) \times f(E_i, \delta_B, \delta_S, \delta_R) - \vec{d}_i$$

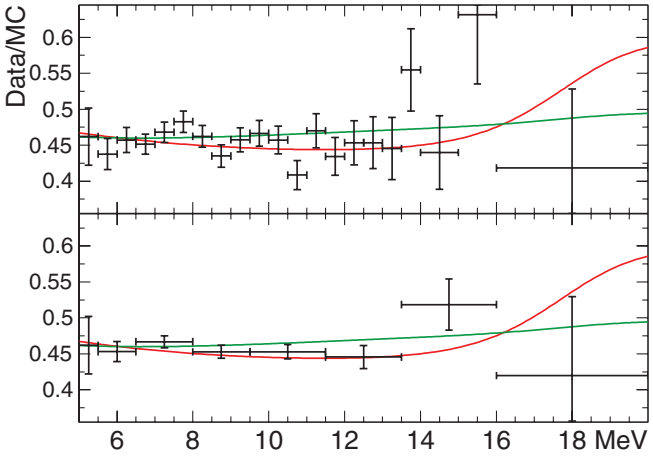

FIG. 51 (color). Distortion of the recoil electron spectrum using 21 (upper panel) and 8 (lower panel) bins. The measured event rates in each bin are divided by the event rates expected from MC assuming a ^{8}B ν flux of 5.076×10^6/ cm^2 s and a hep ν flux of 32×10^3/ cm^2 s. Overlaid is a typical LMA solution (red) and a LOW solution (green), where the assumed neutrino fluxes were fit to best describe the data.

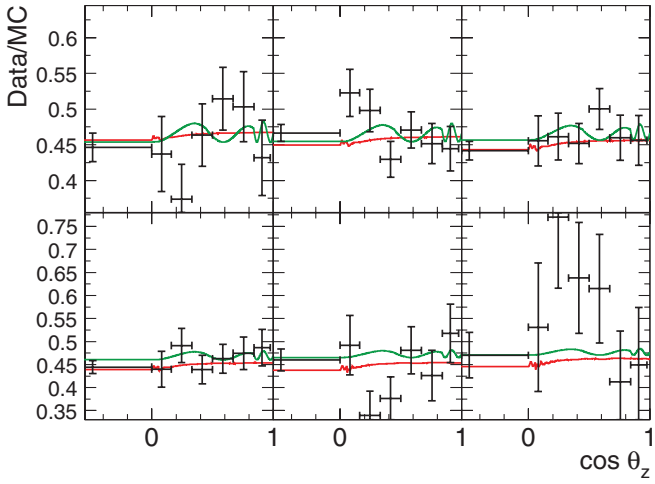

FIG. 52 (color). Dependence of data/MC on solar zenith angle. The MC assumes a ^{8}B ν flux of 5.076×10^6/ cm^2 s and a hep ν flux of 32×10^6/ cm^2 s. The six panels correspond to the energy ranges 5.5–6.5 MeV, 6.5–8.0 MeV, 8.0–9.5 MeV, 9.5–11.5 MeV, 11.5–13.5 MeV, and 13.5–16.0 MeV. Overlaid is a typical LMA solution (red) and a LOW solution (green), where the assumed neutrino fluxes were fit to best describe the data.

allows for arbitrary total neutrino fluxes through the free parameters β and η. The combined rate predictions $\beta\vec{b}_i + \eta\vec{h}_i$ are modified by the energy-shape factors

$$f(E_i, \delta_B, \delta_S, \delta_R) = f_B(E_i, \delta_B) \times f_S(E_i, \delta_S) \times f_R(E_i, \delta_R)$$

with δ_B describing the ^{8}B neutrino spectrum shape uncertainty, δ_S describing the uncertainty of the SK energy scale (0.64%) and δ_R describing the uncertainty of the SK energy resolution (2.5%). The $n \times n$ matrices V_i (n is the number of zenith angle bins) describe statistical and energy-uncorrelated systematic uncertainties. Those systematic uncertainties are assumed to be fully correlated in zenith angle.

To construct the V_i, we transform the rate vectors from the zenith angle basis to a new basis: the first component gives the average rate, the second component the day/night difference, the third component the difference between the rate of the mantle 1 bin and the other night bins, etc. This is achieved by multiplying $\vec{\Delta}_i$ by the nonsingular matrix S which depends on the livetimes of each zenith angle bin: $\vec{\Delta}_i' = S \cdot \vec{\Delta}$

$$S = \begin{pmatrix} L_1/L_{1\to n} & L_2/L_{1\to n} & \cdots & L_n/L_{1\to n} \\ -1 & L_2/L_{2\to n} & \cdots & L_n/L_{2\to n} \\ 0 & -1 & \cdots & L_n/L_{3\to n} \\ \vdots & \vdots & \cdots & \vdots \\ 0 & \cdots & -1 & 1 \end{pmatrix},$$

where L_z is the livetime of zenith angle bin z and $L_{z\to n} = \sum_{z'=z}^{n} L_{z'}$. The χ^2 quadratic form $\vec{\Delta}_i^T \cdot V_i^{-1} \cdot \vec{\Delta}_i$ transforms as $V_i' = S \cdot V_i \cdot S^T$ $((S \cdot V_i \cdot S^T)^{-1} = S^{T-1} \cdot V_i^{-1} \cdot S^{-1})$. Since in this new basis, the first component of $\vec{\Delta}_i'$ is the livetime-averaged rate difference of energy bin i, the energy-uncorrelated systematic uncertainties $\sigma_{i,u}^2$ (assumed to be fully correlated in zenith angle) can simply be added to the statistical uncertainties $S \cdot V_{i,\text{stat}} \cdot S^T$:

$$S \cdot V_i \cdot S^T = S \cdot V_{i,\text{stat}} \cdot S^T + \begin{pmatrix} \sigma_{i,u}^2 & 0 & \cdots & 0 \\ 0 & 0 & \cdots & 0 \\ \vdots & \vdots & \cdots & \vdots \\ 0 & 0 & \cdots & 0 \end{pmatrix}.$$

Of course, $V_{i,\text{stat}}$ is diagonal. If $\sigma_{i,u}$ is asymmetric, two error matrices V_{i+} and V_{i-} are constructed. The sign of $\Delta_{i,1}'$ (livetime-averaged rate difference) decides if $\vec{\Delta}_i^T \cdot V_{i+}^{-1} \cdot \vec{\Delta}_i$ or $\vec{\Delta}_i^T \cdot V_{i-}^{-1} \cdot \vec{\Delta}_i$ contributes to the χ^2

$$\chi_0^2 = \sum_{i=1}^{m} \vec{\Delta}_i^T \cdot V_i^{-1} \cdot \vec{\Delta}_i. \tag{9.2}$$

For any given parameters δ_k, χ_0^2 is just a quadratic form in the neutrino flux factors β and η and can be written as

$$\chi_0^2 = \chi_m^2 + \vec{\Phi}^T C_0 \vec{\Phi} \quad \text{with} \quad \phi = \begin{pmatrix} \beta - \beta_{\min} \\ \eta - \eta_{\min} \end{pmatrix},$$

where the 2×2 curvature matrix C_0 is the inverse of the covariance matrix for β and η. This matrix C_0 must therefore be inversely proportional to the combined uncertainty of all data bins:

$$\frac{1}{\sigma_0^2} = \sum_{i=1}^{m} \frac{1}{\sigma_{\text{stat},i}^2 + \sigma_{i,u}^2} \quad \text{with} \quad \frac{1}{\sigma_{\text{stat},i}^2} = \sum_{z=1}^{n} \frac{1}{\sigma_{\text{stat},i,z}^2}.$$

However, the energy-uncorrelated systematic uncertainties $\sigma_{i,u}$ do not reflect the total uncertainty of the SK rate. For example, the uncertainty in the fiducial volume due to a systematic vertex shift cancels for the spectrum shape and is therefore not included in $\sigma_{i,u}$. If the spectrum data is used to constrain the total rate, the total uncertainty of that rate (σ_0) therefore neglects that part (called σ_r) of the systematic uncertainty which cancels for the spectrum. While σ_r is fully correlated in both energy and zenith angle, it is not covered by the energy-correlated uncertainties either, which reflect only the uncertainties in the ^{8}B neutrino spectrum, the SK energy scale, and the SK energy resolution. To take σ_r into account χ_0^2 is modified to

$$\chi_1^2 = \chi_m^2 + \vec{\Phi}^T C_1 \vec{\Phi} \quad \text{with} \quad C_1 = \frac{\sigma_0^2}{\sigma_0^2 + \sigma_r^2} \times C_0,$$

which has the same minimum as χ_0^2 but allows an enlarged range of parameters β, η. The total χ^2 for the SK zenith spectrum shape is then

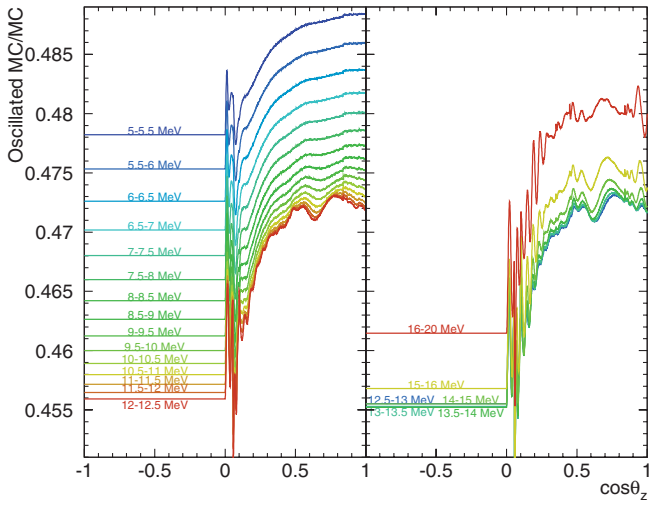

FIG. 53 (color). Predicted solar zenith angle variation assuming a typical LMA solution, $\Delta m^2 = 6.3 \times 10^{-5}$ eV^2 and $\tan^2\theta = 0.52$ (which is the best fit to the SK energy spectrum, rate, and day/night variation).

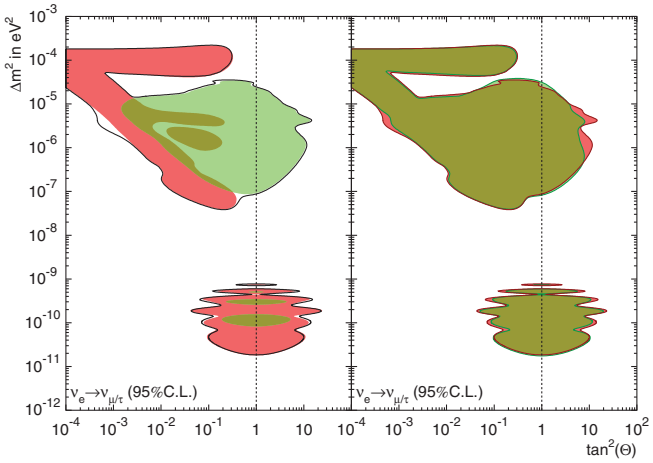

FIG. 54 (color). Left: excluded regions from the SK spectrum (red), SK rate time variations (green), and both combined (solid line) at 95% C.L. Right: excluded regions from the SK zenith spectrum (green) compared to the SK spectrum combined with the time-variation likelihood (red) at 95% C.L.

$$\chi^2_{\rm SK} = \min\left(\chi^2_1(\beta, \eta, \delta_B, \delta_S, \delta_R) + \left(\frac{\delta_B}{\sigma_B}\right)^2 + \left(\frac{\delta_S}{\sigma_S}\right)^2 + \left(\frac{\delta_R}{\sigma_R}\right)^2\right), \tag{9.3}$$

where all δ_k as well as β, η are minimized. To constrain the ^{8}B flux, the term $(\frac{\beta-1}{\sigma_f})^2$ is added.

C. Unbinned time-variation analysis

In a different approach to combine time-variation and spectrum constraints we form the total likelihood $\mathcal{L}$ modifying the solar signal factors s_{ij} of Eq. (8.1) to

$$s_{ij} = p(\cos\theta_{ij}, E_j) \times \frac{r_i(t_j)}{r_i^{\rm av}}, \tag{9.4}$$

where t_j is the event time, $r_i(t)$ the predicted time dependence of the solar neutrino interaction rate in energy bin i, and $r_i^{\rm av}$ the predicted time-averaged rate. Figure 53 shows the expected solar zenith angle dependence $r_i(\cos\theta_z)$ in each energy bin for a typical LMA solution. The recoil electron spectrum enters this likelihood through the weight factors Y_i of Eq. (8.1), so the likelihood needs to add terms like those in Eq. (9.3) to account for energy-correlated systematic uncertainties. The definition of energy bins is the same as in Eq. (8.1): This analysis uses 21 energy bins compared to 8 energy bins for the zenith spectrum.

Because of the large number of solar neutrino candidates, the maximization of this likelihood is too slow to be practical. We therefore split it into

$$\log\mathcal{L} = (\log\mathcal{L} - \log\mathcal{L}_{\rm av}) + \log\mathcal{L}_{\rm av},$$

where $\mathcal{L}_{\rm av}$ is the likelihood without the time variations, which means that it depends only on the average rates in each recoil electron energy bin. We can cast this in terms of a $\chi^2 = -2\log\mathcal{L}$:

$$\chi^2 = \Delta\chi^2_{\rm tv} + \chi^2_{\rm av} \quad \text{with} \quad \Delta\chi^2_{\rm tv} = -2(\log\mathcal{L} - \log\mathcal{L}_{\rm av}). \tag{9.5}$$

The first term of $\Delta\chi^2_{\rm tv}$ uses the time-dependent solar signal factors of Eq. (9.4) while the second term is the same as Eq. (8.1). The spectrum weights Y_i occurring in that equation are determined from the oscillated predicted spectrum. This predicted spectrum is formed using the ^{8}B and hep neutrino fluxes as well as the systematic uncertainty parameters δ_B, σ_B, and δ_S. The values of these five parameters result from a fit to the (time-averaged) SK spectrum data. The dark gray areas in Fig. 54 are excluded at 95% C.L. by this $\Delta\chi^2_{\rm tv}$.

All systematic uncertainties are assumed to be fully correlated in zenith angle or any other time-variation variable. Since the sensitivity is dominated by statistical uncertainties, this assumption is not a serious limitation. We found the statistical likelihood in each energy bin i to be very close to a simple Gaussian form, so $\chi^2_{\rm av}$ takes the same form as Eq. (9.3) but replacing Eq. (9.2) with

$$\chi^2_0 = \sum_{i=1}^{N_{\rm bin}} \left(\frac{\Delta_i}{\sigma_i}\right)^2, \tag{9.6}$$

where Δ_i has only one zenith angle bin (between $-1 < \cos\theta_z < 1$)

$$\Delta_i(\beta, \eta) = (\beta \cdot b_i + \eta \cdot h_i) \times f(E_i, \delta_B, \delta_S, \delta_R) - d_i,$$

and $\sigma_i^2 = \sigma_{i,\rm stat}^2 + \sigma_{i,u}^2$ is the total energy-uncorrelated uncertainty in that bin. The regions colored in red in Fig. 54 are excluded at 95% C.L. using $\chi^2_{\rm av}$ without the term constraining the ^{8}B neutrino flux.

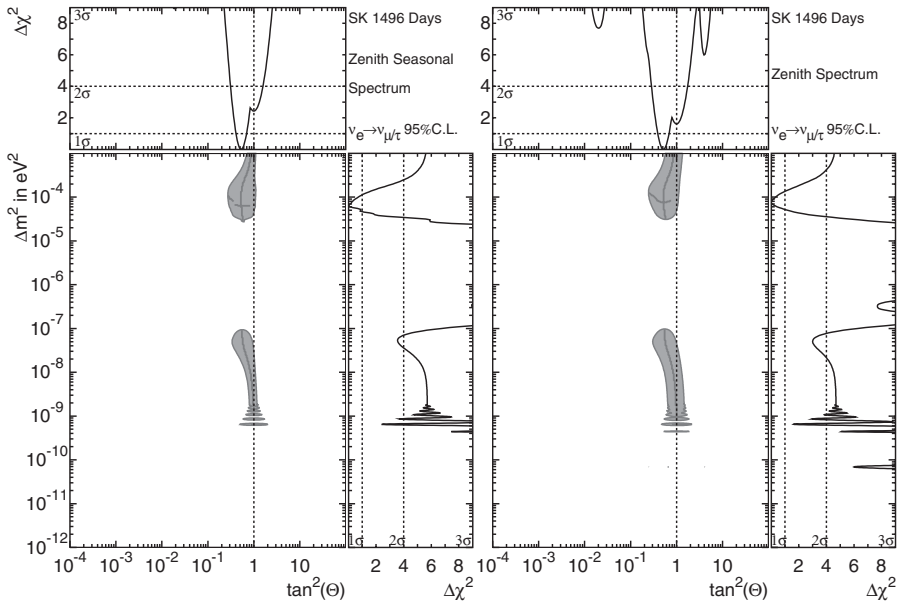

FIG. 55. Allowed areas from the rate-constrained SK unbinned time-variation analysis (left) and the SK zenith spectrum (right) at 95% C.L. The graphs at the top (and right) show the χ^2 difference as a function of $\tan^2\theta$ (Δm^2) alone where the Δm^2 ($\tan^2\theta$) is chosen to minimize χ^2. The lines inside the contours show which Δm^2 ($\tan^2\theta$) is chosen.

D. Oscillation constraints from SK

The combined excluded areas (from $\chi^2 = \chi^2_{\rm av} + \Delta\chi^2_{\rm tv}$) at 95% C.L. are shown inside the solid line in the left panel of Fig. 54. The right panel of the same figure compares these areas to the excluded areas from the zenith spectrum analysis. Both contours are quite similar, however the unbinned time-variation analysis has more stringent limits on the time variation (note the region 10^{-6} eV$^2 < \Delta m^2 < 10^{-5}$ eV^2 at $\tan^2\theta \approx 10^{-3}$ and $\tan^2\theta > 1$). Because of the larger number of energy bins, the likelihood analysis has also larger excluded areas in the vacuum region and at $\Delta m^2 \approx 10^{-4}$ eV^2. If we include the last term in Eq. (9.6), we get the allowed regions (95% C.L.) shown in Fig. 55 which depend on the total ^{8}B neutrino flux measurement of

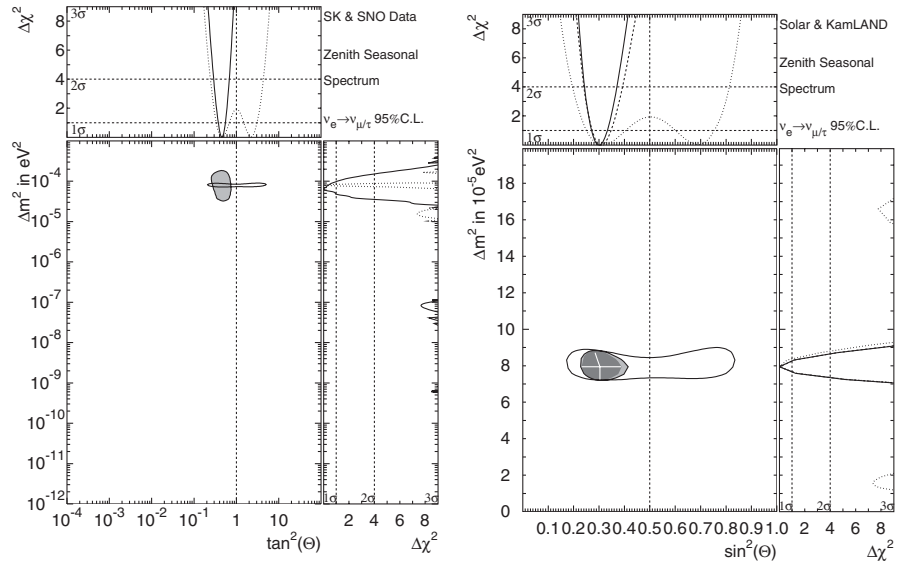

FIG. 56. (a) Allowed area at 95% C.L. from the combination of SK and SNO. Overlaid is the area allowed by KamLAND data. The graphs at the top (right) show the χ^2 difference as a function of only $\tan^2\theta$ (Δm^2); the solid line is the SK/SNO fit, the dotted line is based on KamLAND [20] data. (b) Allowed area at 95% C.L. from the combination of SK/SNO (gray) and all solar data (dark gray) with KamLAND results. The lines inside the contours show the best-fit Δm^2 ($\tan^2\theta$) given a particular $\tan^2\theta$ (Δm^2). Note the linear scale on both axes. Only LMA-I remains allowed.

SNO [18]. The best fit is in the LMA region at $\tan^2\theta = 0.52$ and $\Delta m^2 = 6.3 \times 10^{-5}$ eV^2 ($\Delta m^2 = 7.6 \times 10^{-5}$ eV^2) for the unbinned time-variation analysis (zenith spectrum analysis) where a day/night asymmetry of -2.1% (-1.5%) is expected and $-1.8 \pm 1.6\%$ ($-1.7 \pm 1.6\%$) is found. (Here, the uncertainties do not include systematic effects.) The χ^2 is 17.3 for 20 degrees of freedom (63% C.L.). The ^{8}B flux is fit to 4.91×10^6/ cm^2 s. The $\chi^2_{\rm av}$ of the SK spectrum and rate is 18.5 for 20 degrees of freedom (55% C.L.). The χ^2 analysis of the zenith spectrum gives a minimum χ^2 of 39.0 with 43 degrees of freedom (65% C.L.). The ^{8}B flux is fit to 4.86×10^6/ cm^2 s. Figure 55 also shows the χ^2 as a function of $\tan^2\theta$ alone where a Δm^2 is chosen for each $\tan^2\theta$ to minimize χ^2: SK data excludes small mixing at more than 3σ. SK data also disfavors $\Delta m^2 > 10^{-3}$ eV^2 and 2×10^{-9} eV$^2 < \Delta m^2 < 3 \times 10^{-5}$ eV^2 (see the plot in the right panel, where χ^2 is minimized with respect to $\tan^2\theta$). Again, the unbinned time-variation analysis has more stringent oscillation constraints and favors the LMA region more strongly.

E. Combined oscillation constraints from several experiments

Stronger constraints on Δm^2 result from the combination of the SK measurements with other solar neutrino data. The 95% C.L. allowed region of Fig. 56 includes in addition to the SK data the SNO measurements of the charged-current interaction rate (and day/night asymmetry) of solar electron neutrinos with deuterons [19]; only LMA solutions survive. Overlaid are the contours allowed by the KamLAND reactor neutrino spectrum [20]. Figure 56 shows the allowed contours of a combined fit to SK, SNO, and KamLAND data. SK and SNO remove the ambiguities in Δm^2 and $\tan^2\theta$ of KamLAND and tighten the constraint on the mixing angle. When the charged-current rates measured by Homestake, GALLEX, and SAGE [21] are included as well, the allowed LMA solutions are further reduced. However, in this case the fit relies on the SSM predictions of the pp, pep, CNO and ^{7}Be neutrino fluxes.

F. Solar day/night effect

Even though KamLAND provides by far the best constraint on the solar Δm^2, it is interesting to study the solar constraints as well. The upper bound arises from the ratios of the electron-neutrino elastic scattering rate in SK, the charged-current neutrino interactions in SNO and Homestake, and the neutral-current neutrino interactions in SNO. The lower bound is due to the solar neutrino day/night effect. As described in [15], we fit the amplitude of this variation to our data and compare it to the expected amplitude. For this fit, only the amplitude of the day/night variation is varied, the *shape* is fixed to the calculated shape for a particular Δm^2 and $\tan^2\theta$ (see Fig. 53 for a typical LMA solution). Demanding consistency between expected and observed amplitude, we obtain a range of 5×10^{-5} eV$^2 < \Delta m^2 < 12 \times 10^{-5}$ eV^2 at the 1σ level and a lower bound of 3×10^{-5} eV$^2 < \Delta m^2$ at the 2σ level ($\tan^2\theta = 0.44$). This agrees very well with the KamLAND measurement of 7.9×10^{-5} eV^2. Conversely, if we confine Δm^2 to the 3σ range 7×10^{-5} eV$^2 < \Delta m^2 < 9 \times 10^{-5}$ eV^2 allowed by KamLAND, the amplitude fit varies only very slightly. In that range the measured SK day/night variation amplitude corresponds to a day/night asymmetry of $-1.7\% \pm 1.6\%(\text{stat})^{+1.3}_{-1.2} \times (\text{syst}) \pm 0.04\%(\Delta m^2)$ while the expected asymmetry ranges from -1.7% to -1.0%. At the SK best-fit $\Delta m^2 = 6.3 \times 10^{-5}$ eV^2, the day/night amplitude fit corresponds to the asymmetry $-1.8\% \pm 1.6\%(\text{stat})^{+1.3}_{-1.2}(\text{syst})$.

X. CONCLUSION

Solar neutrino measurements using neutrino-electron scattering in the Super-Kamiokande detector are described. We obtained 1496 effective days of data in the time period of May 31, 1996, through July 15, 2001. The analysis threshold was 6.5 MeV for the first 280 days, and 5.0 MeV for the remaining 1216 days. The observed interaction rate corresponds to a ^{8}B solar electron-neutrino flux of $2.35 \pm 0.02 \pm 0.08 \times 10^6$ cm^{-2} sec^{-1}. We searched for periodic time variations of this rate and found only the expected seasonal variation caused by the eccentricity of the Earth's orbit. The energy spectrum of the recoiling

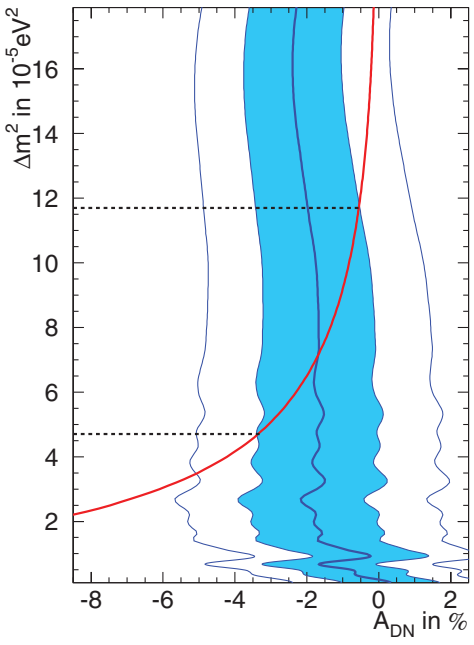

FIG. 57 (color). Day/Night amplitude fit depending on Δm^2. The fit depends only very weakly on the mixing angle which is assumed to be $\tan^2\theta = 0.44$. Overlaid (red line) is the expected amplitude and (blue lines) the 2σ boundaries of the amplitude fit.

electron is consistent with an undistorted solar ^{8}B neutrino spectrum. Based on these results the solar neutrino oscillation analysis imposes strong constraints on the oscillation parameters, selecting large mixing and favoring the large mixing angle solution. The combination with data from other experiments confirms the large mixing angle solution and further reduces the uncertainty in the oscillation parameters. Demanding consistency between expected and observed amplitude, we obtain a range of 5×10^{-5} eV$^2 < \Delta m^2 < 12 \times 10^{-5}$ eV^2 at the 1σ level and a lower bound of 3×10^{-5} eV$^2 < \Delta m^2$ at the 2σ level ($\tan^2 = 0.44$) as shown in Fig. 57.

ACKNOWLEDGMENTS

The authors acknowledge the cooperation of the Kamioka Mining and Smelting Company. Super-Kamiokande has been built and operated from funding by the Japanese Ministry of Education, Culture, Sports, Science and Technology, and the United States Department of Energy, and the U.S. National Science Foundation. Some of us have been supported by funds from the Korean Research Foundation (BK21) and the Korea Science and Engineering Foundation, the State Committee for Scientific Research in Poland (Grants No. 1P03B08227 and No. 1P03B03826), and Japan Society for the Promotion of Science.

[1] S. Fukuda *et al.*, Nucl. Instrum. Methods Phys. Res., Sect. A **501**, 418 (2003).
[2] H. Kume *et al.*, Nucl. Instrum. Methods Phys. Res. **205**, 299 (1983).
[3] A. Suzuki *et al.*, Nucl. Instrum. Methods Phys. Res., Sect. A **329**, 299 (1993).
[4] C. E. Ortiz *et al.*, Phys. Rev. Lett. **85**, 2909 (2000).
[5] J. N. Bahcall *et al.*, Phys. Rev. C **54**, 411 (1996).
[6] J. N. Bahcall *et al.*, Phys. Rev. D **51**, 6146 (1995).
[7] J. N. Bahcall and M. H. Pinsonneault, Phys. Rev. Lett. **92**, 121301 (2004).
[8] A. Morel *et al.*, Limnology and Oceanography **22**, 709 (1977).
[9] M. Nakahata *et al.*, Nucl. Instrum. Methods Phys. Res., Sect. A **421**, 113 (1999).
[10] E. Blaufuss *et al.*, Nucl. Instrum. Methods Phys. Res., Sect. A **458**, 636 (2001).
[11] M. Nemoto *et al.*, Radioisotopes **46**, 710 (1997).
[12] Y. Takeuchi *et al.*, Nucl. Instrum. Methods Phys. Res., Sect. A **421**, 334 (1999).
[13] C. Mitsuda *et al.*, Nucl. Instrum. Methods Phys. Res., Sect. A **497**, 414 (2003).
[14] Y. Takeuchi *et al.*, Phys. Lett. B **452**, 418 (1999).
[15] M. B. Smy *et al.*, Phys. Rev. D **69**, 011104 (2004).
[16] S. P. Mikheyev and A. Y. Smirnov, Sov. J. Nucl. Phys. **42**, 913 (1985); L. Wolfenstein, Phys. Rev. D **17**, 2369 (1978).
[17] A. M. Dziewonski and D. L. Anderson, Phys. Earth Planet. Inter. **25**, 297 (1981).
[18] B. Aharmim *et al.* (SNO Collaboration), Phys. Rev. C **72**, 055502 (2005); S. N. Ahmed *et al.*, Phys. Rev. Lett. **92**, 181301 (2004).
[19] Q. R. Ahmed *et al.*, Phys. Rev. Lett. **89**, 011301 (2002); **89**, 011302 (2002).
[20] T. Araki *et al.* (KamLAND Collaboration), Phys. Rev. Lett. **94**, 081801 (2005).
[21] B. T. Cleveland *et al.*, Astrophys. J. **496**, 505 (1998); J. N. Abdurashitov *et al.*, Phys. Rev. C **60**, 055801 (1999); M. Altmann *et al.*, Phys. Lett. B **490**, 16 (2000); C. Cattadori, Proceedings of Neutrino 2004.